

A 3D radiation-hydrodynamic AGB binary model

ZHUO CHEN,¹ NATALIA IVANOVA,¹ AND JONATHAN CARROLL-NELLENBACK²

¹*Department of Physics, University of Alberta, Edmonton, AB T6G 2E1, Canada*

²*Department of Physics and Astronomy, University of Rochester, Rochester, NY 14627, USA*

ABSTRACT

The origin of the chemically peculiar stars and non-zero eccentricity in evolved close binaries have been long-standing problems in stellar evolution. Answers to these questions may trace back to an intense mass transfer phase. In this work, we use **AstroBEAR** to solve the 3D radiation-hydrodynamic equations and calculate the mass transfer rate in asymptotic-giant-branch (AGB) binaries that undergo the wind-Roche-lobe-overflow or Bondi-Hoyle-Lyttleton (BHL) accretion. To resolve the dynamics of a circumbinary disk, we implement an azimuthal angle-dependent 3D radiation transfer. We consider optically thin cooling and obtain the number density of the coolants by solving the Saha equation. We use **MESA** to produce the density and temperature of the boundary condition of the AGB star. Four simulations are carried out to illustrate the transition from the wind-Roche-lobe-overflow to BHL accretion. Both circumbinary disks and spiral structure outflows can appear in the simulations. The resulting mass transfer efficiency in our models is up to a factor of eight times higher than what the standard BHL accretion scenario predicts, and the outflow gains up to 91% of its initial angular momentum when it reaches 1.3 binary separations. Consequently, some AGB binaries may undergo orbit shrinkage, and some will expand. The mass transfer efficiency is closely related to the presence of the circumbinary disks. Circumbinary disks may form when the optical thickness in the equatorial region becomes greater than a critical value. The increase of the optical thickness is due to the deflected wind.

Keywords: binaries: symbiotic – methods: numerical – stars: AGB and post-AGB – stars: winds, outflows

1. INTRODUCTION

Asymptotic-giant-branch (AGB) stars have a significantly larger size (~ 1 AU) than their main-sequence counterparts. They have pulsating atmosphere (Vlemmings et al. 2017; Khouri et al. 2019) and may exhibit variability with a long period from 200 days to 1000 days (Mowlavi et al. 2018; Karambelkar et al. 2019). AGB stars are one of the major sites in galaxies that produce metal. Metal can be carried away from the AGB stars by radiation-driven AGB winds when dust form. Such properties make the AGB stars ideal for interacting with, more specifically, pollute their

nearby stellar objects. In the case that there is a main-sequence star close to an AGB star, a substantial fraction of the mass-loss may be accreted onto the main sequence companion (Mohamed & Podsiadlowski 2012; Chen et al. 2017; de Val-Borro et al. 2017; Saladino et al. 2018). As a result, the metallicity of the companion may change. Such early-stage low-mass stars become chemically peculiar, and their future evolution will be strongly affected. Carbon-enhanced-metal-poor (CEMP) stars (Abate et al. 2013, 2015), Barium stars (Bidelman & Keenan 1951; Escorza et al. 2019), CH stars (Keenan 1942; McClure & Woodsworth 1990) and dwarf carbon (Dahn et al. 1977; Roulston et al. 2019) are common examples of the chemically peculiar stars. Their existence could be the evidence of the mass transfer during the previous AGB binary phase. The binarity of CH stars and CEMP stars has been studied through long-term observation (McClure & Woodsworth 1990; Jorissen et al. 2016), confirming that many of them have

Corresponding author: Zhuo Chen
 zc10@ualberta.ca

Corresponding author: Natalia Ivanova
 nata.ivanova@ualberta.ca

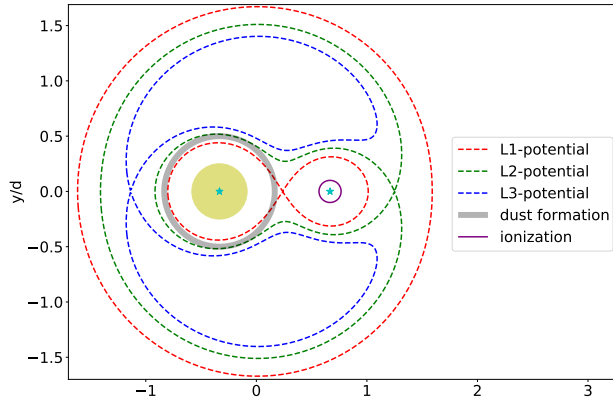


Figure 1. A schematic picture of the WRLOF. The coordinate is scaled to the binary separation d . The contours of the L1, L2, and L3 Lagrangian potential are drawn in red, green, and blue dashed lines. The AGB star is in yellow color, which is filling a fraction of its Roche lobe. Its dust forming region is represented by the gray ring. The companion star may have an ionization region, and we indicate that region by a purple line.

companions. A strong positive correlation between the circumstellar disk and binarity has also been established in galactic RV Tauri stars (Manick et al. 2017). The non-zero eccentricity in these stars indicates some intense interactions that can pump the eccentricity may happen in close binary with giants. Also, many RV Tauri stars show a lack of refractory elements, which is called ‘depletion’ (Giridhar et al. 1994; Van Winckel et al. 1998). Some researches suggest that the reaccretion of gas from a circumstellar disk around the post-AGB star (Gezer et al. 2019; Oomen et al. 2019) may induce the ‘depletion.’ Besides the ‘smoking gun’ evidence, observations also reveal that dusty circumbinary disks exist in binary systems with evolved stars (Kervella et al. 2015; Hillen et al. 2016; Homan et al. 2017; Ertel et al. 2019). UV excess of some AGB stars also implies that there could be accreting main-sequence companions near them (Sahai et al. 2008; Ortiz & Guerrero 2016).

In close AGB binaries, the mass transfer efficiency almost dictates the intensity of the interaction between the two stars. However, it has been a difficult problem to quantify the mass transfer efficiency observationally because of the uncertainty in the measurement of the mass-loss rate and accretion rate. The difficulty in observation makes the first principle numerical simulation an ideal approach to quantify the mass transfer efficiency. Figure 1 shows a schematic picture of an AGB binary undergoing wind-Roche-lobe-overflow (WRLOF) as described in Podsiadlowski & Mohamed (2007). The difference between the WRLOF and Roche-lobe overflow (RLOF) is that the AGB star is not filling its

Roche-lobe to the full. On the other hand, if the binary separation is so significant that the dust formation region is much smaller than the Roche lobe of the AGB star, the mass transfer mechanism approaches the Bondi-Hoyle-Lyttleton (BHL) accretion limit (Hoyle & Lyttleton 1939; Bondi & Hoyle 1944; Edgar 2004). In that scenario, the radiation driven AGB wind becomes supersonic before it crosses the Roche lobe of the AGB star. The two stars become not causally connected by hydrodynamics. The secondary may accrete mass from the AGB wind without imposing much effect on the AGB star’s atmosphere. Such a scenario has been carefully investigated in simulations that focus on the hydrodynamics around the secondary (Huarte-Espinosa et al. 2013). Although we qualitatively know that WRLOF is different from the BHL accretion, the transition from the WRLOF to the BHL accretion is still poorly understood. One goal of this research is to illustrate such a transition with incremental change of the binary separation.

Dust formation is the key to model the mass transfer process in AGB binaries. When dust form, the opacity of the fluid may increase by a factor of 10^4 , and the outflow may become supersonic in a short time under the radiation pressure. The location of the dust formation region almost determines the domain of dependence (circumbinary disk scenario is an exception) of both stars and the mass transfer mechanism. The dust formation problem has been studied from a kinetic perspective by modeling the dust growth and sublimation from clusters of small particles (Gail et al. 1984; Gail & Sedlmayr 1985, 1986, 1988). The method has been used by Helling & Woitke (2006) to study the dust in brown dwarfs and applied to the AGB wind problem in 1D (Jeong et al. 2003), 2D (Woitke 2006a,b), and 3D (Freytag & Höfner 2008; Höfner & Freytag 2019). This first principle approach is invaluable because the dust formation and destruction are susceptible to the radiation and hydrodynamical environment. However, an accurate (and sensitive) dust formation model would intrinsically require other parts of physics to be as accurate. Unfortunately, radiative transfer, chemistry, and hydrodynamics around AGB stars are all in complicated situations and likely to be coupled.

The chemistry plays a vital role in the formation of dust and the dynamics of AGB winds. Boulanger et al. (2019a) modeled the AGB atmospheres and the AGB winds in a dust-free and radiation-free environment. They emphasize the chemical non-equilibrium nature around the AGB stars and conclude that the chemical processes may regulate the thermodynamics of the AGB stars’ atmosphere, thus strongly affect the properties of

the winds. Recently, [Boulangier et al. \(2019b\)](#) endeavored to model the onset of nucleation process from the non-equilibrium chemical reaction. The nucleation process may explain the origin of the small particles in the kinetic model. However, the biggest obstacle of such an approach is the lack of quantitative information about some reaction rates.

The radiation in the atmosphere of an AGB star may not be in local thermal equilibrium (LTE) with the gas, and the scattering of the radiation may also be non-negligible. [Woitke \(2006a\)](#) solved the radiative transfer problem in their 2D model with the Monte Carlo method. Although [Woitke \(2006a\)](#) reported a negative result on the formation of the dusty wind, they pointed out that the composition-dependent dust formation and non-gray radiative transfer might play a crucial role if one wants to model the dusty wind correctly. [Freytag & Höfner \(2008\)](#) performed a 3D calculation of the AGB atmosphere with non-local radiation transfer in an explicit scheme. Their results not only exhibited the dust formation in the post-shock region but also showed the AGB winds with reasonable mass-loss rates. In the mean time, radiation-hydrodynamics may affect the dynamics of the circumbinary disks in AGB binaries but is still poorly understood. One critical physics in the circumbinary disk is still the evolution of the dust and the scattering of the radiation.

The equation of state (EoS) problem has not been studied systematically in the context of the WRLOF. In AGB stars' atmosphere, the internal energy change in phase transitions, e.g. $\text{H}_2 \rightleftharpoons \text{H}$ and $\text{H} \rightleftharpoons \text{H}^+ + \text{e}^-$ is significant compared to the kinetic part of thermal energy ([Chen et al. 2019](#)) and radiation energy. [Freytag & Höfner \(2008\)](#) used a Roe-type Riemann solver with a tabulated equation of state to resolve the ionization. Phase transitions such as the dissociation of H_2 and the ionization of H and He take place in the accreting flow, too. These phase transitions are very similar to the ones in star formation, and many similar physical phenomena may happen around the accreting (main-sequence) stars in AGB binaries.

The binary separation and eccentricity would change because of the mass transfer and interaction between the circumbinary disk and binary stars ([Artymowicz & Lubow 1994](#); [Dermine et al. 2013](#); [Saladino & Pols 2019](#)). [Chen et al. \(2018\)](#) studied the change of the binary separation by extracting the information of the mass transfer rate, mass-loss rate, and angular momentum loss rate in their Cartesian grid-based radiation hydrodynamic model ([Chen et al. 2017](#)). SPH method has also been used to study the evolution of the binary separation ([Liu et al. 2017](#); [Saladino et al. 2019](#)) and eccentricity ([Sal-](#)

[adino & Pols 2019](#)). The Cartesian grid-based method is usually not effective in angular momentum conservation. The error in angular momentum conservation is tested and showed not to affect their conclusions in [Chen et al. \(2018\)](#). A better way to conserve the angular momentum in grid-based code is perhaps to use a spherical coordinate mesh. On the other hand, the SPH method usually could not resolve shocks well. In the atmosphere of the AGB star, shocks can levitate the atmosphere to the radius where dust could condensate ([Lamers & Cassinelli 1999](#); [Freytag et al. 2017](#)). Without shocks, the mass-loss rate of AGB winds is usually too low. Another important shock in an AGB binary is the bow shock around the secondary. The region within the bow shock is a domain of dependence of the accretion disk. Material that crosses this bow shock maybe eventually accreted by the secondary.

In this research, we present a 3D radiation hydrodynamic model for the AGB binary system. We carried out Four simulations on the Cedar cluster of Compute Canada.¹ Each simulation costs 20 core years. The rest of this paper is organized as follows: we discuss the adopted physics models in Section 2. Section 3 has the governing equations of our 3D radiation-hydrodynamic binary model. Section 4 discuss the setup of the simulation domain. Section 5 describes the boundary conditions for the AGB star and secondary. The results of the single AGB star, mass transfer efficiency, outflow morphology, outflow angular distribution, and orbital stability can be found in Section 6. We conclude our work and discuss the implications of our results in Section 7.

2. PHYSICS

2.1. Overall setup of the problem

We consider binary systems that consist of an AGB star with a fixed mass of $1.02M_{\odot}$ and a main-sequence star with a fixed mass of $0.51M_{\odot}$. The separation of the binary varies from 5.4 AU to 6.6 AU. This range of orbital separations was found to encapsulate the transition from the WRLOF to BHL accretion, as will be discussed in Section 6.2 and 6.3. The orbit of the binary is considered to be circular.

The stellar model of the primary star is obtained with detailed stellar evolution code and then the stellar model is used as a boundary condition (see §5). Specifically, we use MESA (Modules of Experiments in Stellar Astrophysics), release 10398 ([Paxton et al. 2011, 2013, 2015, 2018](#)). We evolve a $1.5M_{\odot}$ zero-age main-sequence (ZAMS) star with an initial $Z = 0.02$ and $X = 0.7$ until

¹ <https://www.computecanada.ca>

the star has reached its AGB phase. The same hydrogen content is used for the matter expelled from the AGB star. We pick the model in the middle of the fast mass-loss phase when the mass of the star has decreased to $1.02M_{\odot}$. During the mass-loss, the star goes through lengthily episodes of expansions and contractions. The specific model we chose for this work has an effective temperature $T_{\text{eff}} = 2874$ K, luminosity $L_p = 4384 L_{\odot}$ and radius of the photosphere $r_{\text{photo}} = 267 R_{\odot}$.

2.2. Dust formation and destruction

Dust forms about 2-3 stellar radii of the AGB star (Höfner & Olofsson 2018) and may be destroyed near the secondary. We assume that destruction and formation of dust are dependent on the gas density ρ and the gas temperature T , and dust does not exist in the following regions:

1. $T > 10^4$ K.
2. $T_{\text{eq}} > T_{\text{sub}}$, where T_{sub} is the dust sublimation temperature.
3. $\rho > 10^{-15} \text{ g}\cdot\text{cm}^{-3}$ and $T > 2000$ K.

Criterion 1 ensures that there is no dust in the very high-temperature region. In the simulations, strong shocks may raise the temperature to 10^4 K thus destroy the dust.

The physical meaning of criterion 2 is that the dust is removed if its "radiation equilibrium" temperature is higher than the sublimation temperature. By "radiation equilibrium" temperature we mean that spherical dust is heated to the temperature that its blackbody radiation can balance the radiation it absorbs if the emission opacity and the absorption opacity are equal, i.e.,

$$\int_0^{\infty} \kappa_{\lambda} I_{\lambda} \pi a_{\text{dust}}^2 d\lambda = \int_0^{\infty} \kappa_{\lambda} B_{\lambda}(T_{\text{eq}}) 4\pi^2 a_{\text{dust}}^2 d\lambda, \quad (1)$$

where λ , κ_{λ} , I_{λ} , B_{λ} are the wavelength, Planck opacity, incoming radiation intensity, and Planck function, respectively. a_{dust} is the radius of the spherical dust grain. If κ_{λ} is a constant, Equation 1 can be simplified to

$$\int_0^{\infty} I_{\lambda} d\lambda = \int_0^{\infty} 4\pi B_{\lambda}(T_{\text{eq}}) d\lambda. \quad (2)$$

If only short wavelength radiation can be absorbed by the newly formed dust, the fraction of that absorbed radiation can be expressed by

$$\beta = \frac{\int_{\lambda_1}^{\lambda_2} \pi B_{\lambda}(T_{\text{eff}}) d\lambda}{\sigma_{\text{sb}} T_{\text{eff}}^4}. \quad (3)$$

Here σ_{sb} is the Stefan-Boltzmann constant. For $\lambda_1 = 0.01 \mu\text{m}$ and $\lambda_2 = 0.91 \mu\text{m}$, $\beta = 0.1875$. This range

composition	$r_{\text{pyro}}/r_{\text{photo}}$	$r_{\text{pyro}}/r_{\text{photo}}$
$\text{Mg}_{0.5}\text{Fe}_{0.5}\text{SiO}_3$	2.85	2.66
$\text{Mg}_{0.6}\text{Fe}_{0.4}\text{SiO}_3$	3.00	2.79
$\text{Mg}_{0.7}\text{Fe}_{0.3}\text{SiO}_3$	1.71	1.63
$\text{Mg}_{0.8}\text{Fe}_{0.2}\text{SiO}_3$	1.43	1.38

Table 1. The second and third column show the formation radius of the test dust grain whose radius is $a_{\text{dust}} = 0.0535 \mu\text{m}$ and $a_{\text{dust}} = 0.01 \mu\text{m}$, respectively.

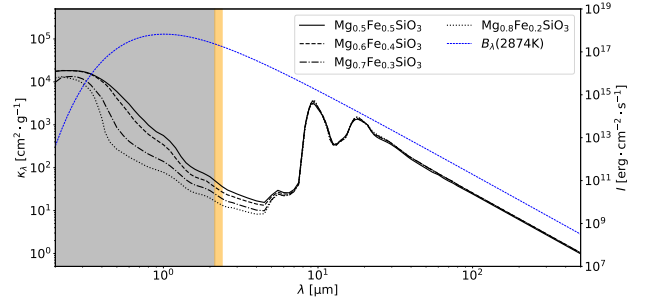


Figure 2. Examples of the wavelength dependence of the absorption opacity of dust. The left y-axis is the opacity and the right y-axis is the radiation power. The black lines show the opacity of different dust species. The blue dashed line shows the black-body spectrum for $T_{\text{eff}} = 2874$ K. Gray band covers the wavelengths $0.01 \leq \lambda \leq 2.15 \mu\text{m}$ and the yellow region covers the wavelengths $2.15 \leq \lambda \leq 2.4 \mu\text{m}$. The shown opacities are found assuming the dust's number density distribution of $dn_{\text{dust}} \approx a_{\text{dust}}^{-3.5}$ for dust radius $0.1 < a_{\text{dust}} < 0.3 \mu\text{m}$ (Mathis et al. 1977).

of wavelengths likely covers the majority of the photons that could be effectively absorbed by the newly formed small ($a_{\text{dust}} < 0.1 \mu\text{m}$) dust grains.

If the material between the AGB star and the dust formation region is transparent, $I_{\lambda} = B_{\lambda}(T_{\text{eff}})$. Make use of Equation 1 and 3 and further assume that κ_{λ} is a constant, we can find

$$T_{\text{eq}} = \left(\frac{\beta L_p}{4\pi\sigma_{\text{sb}} r_p^2} \right)^{0.25}, \quad (4)$$

where r_p is the distance from the dust to the center of the star. A dust formation radius can be calculated if a sublimation temperature T_{sub} is given.

$$r_p = \frac{\sqrt{\beta} T_{\text{eff}}^2 r_{\text{photo}}}{T_{\text{sub}}^2}. \quad (5)$$

When $T_{\text{sub}} = 1300$ K, $r_{\text{dust}} \approx 2.12 r_{\text{photo}}$.

Indeed, κ_{λ} for dust is a function that has a greater value in the short wavelength, see Figure 2 where we show κ_{λ} for pyroxene with different concentration of iron and radii. We use databases of Dust Optical Properties

² for the optical properties of the specific pyroxene composition (Jaeger et al. 1994; Dorschner et al. 1995). The dust opacity is calculated using the Mie model (Mätzler 2002). Pyroxene has a sublimation temperature of about 1500 K (Kobayashi et al. 2011). We use the variable κ_λ and the whole spectrum to find the formation radii for several types of dust grains, see Table 1. We can see that the radius predicted by our simplified dust formation model falls in the range of the formation radius of pyroxene.

In our simulations, r_{dust} is found using the actual incoming intensity. The incoming intensity may be attenuated by the matter between the AGB star and the dust formation region, i.e., it depends on the dust-free optical depth τ , which itself is the function of the direction from the AGB star. As a result, the location of dust formation or destruction depends on the direction from the AGB star and is

$$r_{\text{dust}}(\theta, \phi) = \frac{\sqrt{\beta} T_{\text{eff}}^2 r_{\text{photo}} e^{-\tau(\theta, \phi)}}{T_{\text{sub}}^2}, \quad (6)$$

where θ is the polar angle and ϕ is the azimuthal angle in the spherical coordinate system centered at the AGB star's center (see Appendix A for detail).

The purpose of criterion 3 is to describe dust destruction around the secondary star. As the density gets higher near the secondary, the dust and gas may come into LTE again and the dust sublimates.

Dust formation is a complicated subject – many species forming at different temperatures, the formation sequence matters a lot, and so on (Jeong et al. 2003; Woitke 2006a). We anticipate that our approach is simplified. We note however that our goal is not to study a realistic dust formation but to use a relatively reasonable dust formation model to drive a phenomenologically pulsating AGB wind.

2.3. Dust and its ability to capture radiation

We integrate the blackbody spectrum for $T_{\text{eff}} = 2874\text{K}$ and find that within the band $0.01 \leq \lambda \leq 2.15 \mu\text{m}$ it covers 75% of the total radiation power; the region $2.15 \leq \lambda \leq 2.4 \mu\text{m}$ covers an additional 5%. In this work, we focus on the absorption of small dust grains. In the case that the dust may grow to $1\mu\text{m}$, the reddening of the spectrum may cover the whole K band (Bladh et al. 2013). In summary, the overall momentum contribution of the blackbody radiation beyond the K band is relatively small, as a result, we only take 75% of the incoming radiation energy as the momentum budget that can be transferred to the dust; we hence choose

to use $fL_p = 0.75L_p$ as the luminosity for the momentum transfer.

2.4. Dust opacity

When r_{dust} is known, we use an opacity profile that mimics the dust growth from the dust-free region to the dusty region

$$\kappa = \frac{\kappa_{\text{dust}}}{1 + \exp\left\{-2 \frac{r_p - r_{\text{dust}} - r_{\text{scale}}}{r_{\text{scale}}}\right\}} + \kappa_{\text{mol}}. \quad (7)$$

Here $\kappa_{\text{mol}} = 2.5 \times 10^{-4} \text{cm}^2 \cdot \text{g}^{-1}$ is the dust-free opacity and $\kappa_{\text{dust}} = 6 \text{cm}^2 \cdot \text{g}^{-1}$. $r_{\text{scale}} = 0.16 \text{AU}$ is the adopted length-scale which mimics the dust growth length-scale. We introduce the corresponding radius where the opacity of the dust-gas mixture reaches the half of its maximum

$$r_{\text{half}} = r_{\text{dust}} + r_{\text{scale}} \approx 2.75 \text{AU}. \quad (8)$$

The choice of r_{scale} is empirical but an order of magnitude estimation could be made to justify the choice. In our model, the characteristic speed of a pulsation at the dust formation radius is $v_{\text{ch}} \approx 5 \text{km} \cdot \text{s}^{-1}$. We can estimate the implied timescale for the dust growth as

$$t_{\text{growth}} \approx 2r_{\text{scale}}/v_{\text{ch}} \approx 0.3 \text{ year}. \quad (9)$$

The multiple 2 comes from the fact that the opacity of the fluid grows to half of its maximum in about r_{scale} distance. This value is smaller than the typical dynamical timescale and pulsation period (~ 1 year) of an AGB star. The AGB stars exhibit variation in the optical light-curves with a period of 200-1000 days which implies that the dust formation time should be smaller than the period of the light-curves.

This implied timescale also makes sense if we perform an order of magnitude calculation of the dust formation time. The average density is about $10^{-15} \text{g} \cdot \text{cm}^{-3}$ (see Figure 4) at $r_p = 2.75 \text{AU}$. According to Jeong et al. (2003), consider the ratio of number of dust grains to $n_{\text{H}_2} \approx 10^8 \text{cm}^{-3}$ to be about 10^{-13} in the dust formation shell and TiO_2 to be the nucleation seed. The nucleation timescale will be in the range of $10^4 - 10^8 \text{s}$. Unfortunately, a more accurate estimation could not be done until a quantitative dust growth model is solved.

2.5. Optically thin cooling

We use the following two groups of processes for the cooling process:

1. The rotational and vibrational cooling of H_2 , H_2O , and CO (Neufeld & Kaufman 1993).
2. Cooling due to the collisional ionization, recombination, collisional excitation, and Bremsstrahlung of H and H^+ (Cen 1992).

² <https://www.astro.uni-jena.de/Laboratory/OCDB/index.html>

We set (Neufeld & Kaufman 1993; Lacy et al. 1994)

$$n_{\text{H}_2\text{O}}/n_{\text{H}_2} = 2 \times 10^{-4}, \quad (10)$$

$$n_{\text{CO}}/n_{\text{H}_2} = 2 \times 10^{-4}. \quad (11)$$

In principle, the abundance of molecules cannot be known without carrying out chemical reaction calculations. In the AGB wind, the C/O ratio is vital to the species of the molecules and dust (Höfner & Olofsson 2018). The ratios we adopted in our simulations make sense only for some oxygen-rich AGB stars.

We calculate n_{H^+} , n_{H} , and n_{H_2} by solving the thermal equilibrium problem, i.e., the Saha equation with the local ρ and T (Chen et al. 2019)

$$\text{H} \rightleftharpoons \text{H}^+ + \text{e}^-, \quad (12)$$

$$\text{H}_2 \rightleftharpoons 2\text{H}. \quad (13)$$

In summary, the cooling strength is

$$\dot{\Lambda} = \dot{\Lambda}_{\text{H}_2} + \dot{\Lambda}_{\text{H}_2\text{O}} + \dot{\Lambda}_{\text{CO}} + \dot{\Lambda}_{\text{H,H}^+}. \quad (14)$$

Ideally, optically thin cooling should only be applied to the optically thin region. In this research, we use ρ alone to identify whether an individual cell is optically thick. If $\rho > 10^{-9} \text{ g cm}^{-3}$, we assume such a cell is optically thick and the optically thin cooling will be turned off. However, with such criterion, the vicinity of the accretion disk may become optically thick. The cooling will be halted and the temperature may rise rapidly to more than 10^5 K . To make the temperature profile smoother and keep the accretion process efficient, we keep the cooling mechanism around the secondary (inside the accretion disk). In a real accretion disk, radiation (thermal and non-thermal) should be able to carry away energy. We currently do not have such a consistent method to let the energy goes away, therefore, we keep the simple cooling method. This may lead to an overestimate of the cooling strength inside the accretion disk.

3. GOVERNING EQUATIONS

The governing equations are the compressible Euler equations in a rotating frame with relevant sink and source terms. We solve the radiation hydrodynamic equations by **AstroBEAR** with static mesh refinement (Carroll-Nellenback et al. 2013).

$$\frac{\partial \rho}{\partial t} + \nabla \cdot (\rho \vec{v}) = 0, \quad (15)$$

$$\frac{\partial \rho \vec{v}}{\partial t} + \nabla \cdot (\rho \vec{v} \vec{v}) = -\nabla p + \rho(\vec{a}_{\text{rad}} + \vec{a}_{\text{g}} + \vec{a}_{\text{i}}), \quad (16)$$

$$\frac{\partial E}{\partial t} + \nabla \cdot [\vec{v}(E + p)] = \dot{\Lambda} + \rho \vec{v} \cdot (\vec{a}_{\text{rad}} + \vec{a}_{\text{g}} + \vec{a}_{\text{i}}), \quad (17)$$

where t, ρ, p , and E are the time, density, pressure, and total energy, respectively. \vec{v} is the velocity in the rotating frame. \vec{a}_{rad} , \vec{a}_{g} , \vec{a}_{i} , and $\dot{\Lambda}$ are the acceleration due to the radiative momentum transfer, gravity of the two stars, and inertial force, and the energy change rate due to the optically thin cooling. We will discuss the considered physics in detail in the following subsections. Also, we adopt a perfect gas EoS,

$$p = \frac{\rho k_{\text{b}} T}{\mu m_{\text{amu}}}, \quad (18)$$

$$\epsilon = \frac{p}{(\gamma - 1)\rho}, \quad (19)$$

$$E = \rho(\epsilon + \frac{v^2}{2}), \quad (20)$$

where k_{b} and m_{amu} are the Boltzmann constant and atomic mass unit. The mean atomic weight is $\mu = 1.3$ and the adiabatic index is $\gamma = 5/3$. We solve the hydrodynamics by the HLLC Riemann solver with the corner transport upwind method (Colella 1990) and piece-wise linear reconstruction.

3.1. Gravitational force and inertial force

\vec{a}_{g} is the gravitational acceleration

$$\vec{a}_{\text{g}} = -\frac{G m_{\text{p}} \hat{\mathbf{r}}_{\text{p}}}{r_{\text{p}}^2} - \frac{G m_{\text{s}} \hat{\mathbf{r}}_{\text{s}}}{r_{\text{s}}^2}, \quad (21)$$

where G is the gravitational constant and

$$\vec{\mathbf{r}}_{\text{p}} = \vec{\mathbf{r}} - \vec{\mathbf{l}}_{\text{p}}, \quad (22)$$

$$\vec{\mathbf{r}}_{\text{s}} = \vec{\mathbf{r}} - \vec{\mathbf{l}}_{\text{s}}. \quad (23)$$

Subscript p and s stand for the primary star and the secondary star, respectively. $\vec{\mathbf{l}}_{\text{p}}$, $\vec{\mathbf{l}}_{\text{s}}$, and $\vec{\mathbf{r}}$ are the Cartesian coordinates of the primary, the secondary, and the cell. We choose the origin to be at the center of mass of the binary system. Self-gravity is ignored because the total mass of the ejected material in all of our simulations is less than $5 \times 10^{-5} M_{\odot}$ which is small compared to the mass of the binary stars. The outflows also have some symmetry which may cancel out most of the net effect of self-gravity.

\vec{a}_{i} is the acceleration due to the inertial force in the rotating frame.

$$\vec{a}_{\text{i}} = -2\vec{\Omega}_{\text{b}} \times \vec{v} - \vec{\Omega}_{\text{b}} \times (\vec{\Omega}_{\text{b}} \times \vec{r}), \quad (24)$$

where $\vec{\Omega}_{\text{b}}$ is the pseudovector of the rotating frame. Its magnitude is the angular frequency of the binary system. Throughout our simulations, $\vec{\mathbf{l}}_{\text{p}}$, $\vec{\mathbf{l}}_{\text{s}}$, and $\vec{\Omega}_{\text{b}}$ are kept constant for computational simplicity. That means we do not track the orbital evolution of the binaries in our simulations. We examine this assumption in Section 6.5.

3.2. Radiation force

In this work, we only consider a single interaction between the photon and dust, i.e., we adopt that the photons are destroyed by the dust once they interact with the dust. This is a reasonable approach as the dust temperature is low, the thermal radiation from a dust grain is less likely to be absorbed by another dust grain. On the other hand, scattering by the dust usually only changes the photon's direction by a small angle (Henyey & Greenstein 1941) thus the anisotropy of the radiation from the AGB star would not be strong. Therefore, we only consider the radiation in the radial direction of the AGB star.

\vec{a}_{rad} is the acceleration due to the radiative pressure from the primary star. The radiation force is given by,

$$\vec{a}_{\text{rad}} = \frac{\kappa f L_{\text{p}} e^{-\tau} \hat{\mathbf{r}}_{\text{p}}}{4\pi c r_{\text{p}}^2}. \quad (25)$$

Here c is the speed of light. $\tau(x, y, z)$ is obtained by linearly interpolating $\tau(r, \theta, \phi)$. κ is given by Equation 7. We treat the AGB star as a point radiation source.

3.3. Time-step and control of the integration

Some of the physics we used, e.g., the cooling, may operate on the timescale shorter than the hydro time-step in a few cells. This makes the energy equation stiff. We solve the stiff ODE problem by comparing the 4th and 5th order Runge-Kutta solution and adaptively evolve the time-step (Press & Teukolsky 1992). For each integration step, we only allow a maximum of 20% change in the internal energy, i.e.,

$$\epsilon^{n+1} > 0.8\epsilon^n, \quad (26)$$

here n is the step number of sub-cycle of the integration.

4. THE SIMULATION DOMAIN

We fix the initial mass ($m_{\text{p}} = 1.02M_{\odot}$) of the AGB star and the secondary ($m_{\text{s}} = 0.51M_{\odot}$) in all of the models. We consider four binary separations, $d = 5.4, 5.7, 6.0, 6.6$ AU.

The simulation box is the same for all the models. It is $48\text{AU} \times 48\text{AU} \times 24\text{AU}$ in the x , y , and z directions, respectively. The base resolution of the domain is $60 \times 60 \times 30$ cells and we use five levels of mesh refinement. Each level of mesh refinement doubles the resolution in each dimension. The physical size of the finest cell is $(2.5 \times 10^{-2}\text{AU})^3$.

The actual simulation domain is a cylinder whose axis coincides with the z -axis. The radius and the height of the cylinder are $r_{\text{domain}} = 23.5\text{AU}$ and $h_{\text{domain}} = 24\text{AU}$, respectively. This cylinder is inside the simulation box.

Radially outward supersonic flow in the lab frame is set outside the cylinder. The temperature of the supersonic flow is 1000K and the speed is $15\text{km}\cdot\text{s}^{-1}$. Such supersonic flow ensures that there is no information propagating into the cylinder from its side surface. The boundary condition of the top and bottom surfaces is set diode, i.e., only outgoing flow is allowed.

The refined region around the secondary is two co-axis cylinders, one with five levels of refinement has a height of 0.5AU and a radius of 1.35AU . The second cylinder has four levels of refinement and has a height of 0.7AU and a radius of 2.7AU . We chose such configuration so that the bigger cylinder covers the circularization radius (Frank et al. 2002), and the smaller cylinder encapsulates the accretion disk (checked posterior). The AGB star is resolved by a sphere with four levels of refinement and the radius of the sphere is 2.85AU . The sphere is aimed to resolve the dust forming region. We resolve the equatorial zone by using a cylinder with three levels of mesh refinement. The height and radius of the equator's cylinder are 1.4AU and 22.5AU , respectively.

5. INNER BOUNDARY CONDITIONS

The primary star and the secondary star are two important inner boundaries in our simulations. We discuss their implementations separately.

5.1. Primary star

The primary star is the AGB star. We use the piston model (Bowen 1988) to approximate the pulsating AGB star. The boundary condition of the primary star determines the temperature, density, radius, velocity, and period of the piston. Figure 3 shows the density and temperature profiles of the AGB star as obtained from MESA.

Similar to some other researches, we place the piston below the photosphere at $R = 247R_{\odot}$ (Bowen 1988; Liljegren et al. 2016). At this radius, MESA model has $T = 9484\text{K}$ and $\rho = 4.77 \times 10^{-9}\text{g}\cdot\text{cm}^{-3}$. The profiles and location of the piston determine the temperature and the density of the piston, which are kept constant throughout the simulations. The sound speed of the piston is roughly $10\text{km}\cdot\text{s}^{-1}$. We adopt a subsonic piston model, the radial velocity of the fluid inside the AGB star is described by

$$v_{\text{piston}}(r_{\text{p}}, t) = \frac{r_{\text{p}}}{R} v_{\text{amp}} \sin\left(\frac{2\pi t}{P_{\text{piston}}}\right) \quad r_{\text{p}} \leq R, \quad (27)$$

where $v_{\text{amp}} = 9\text{km}\cdot\text{s}^{-1}$ is the amplitude of the piston and $P_{\text{piston}} = 1\text{yr}$ is the adopted period of the piston. The v_{amp} we choose corresponds to 0.9Mach . We have tested smaller amplitude and find that the subsequent

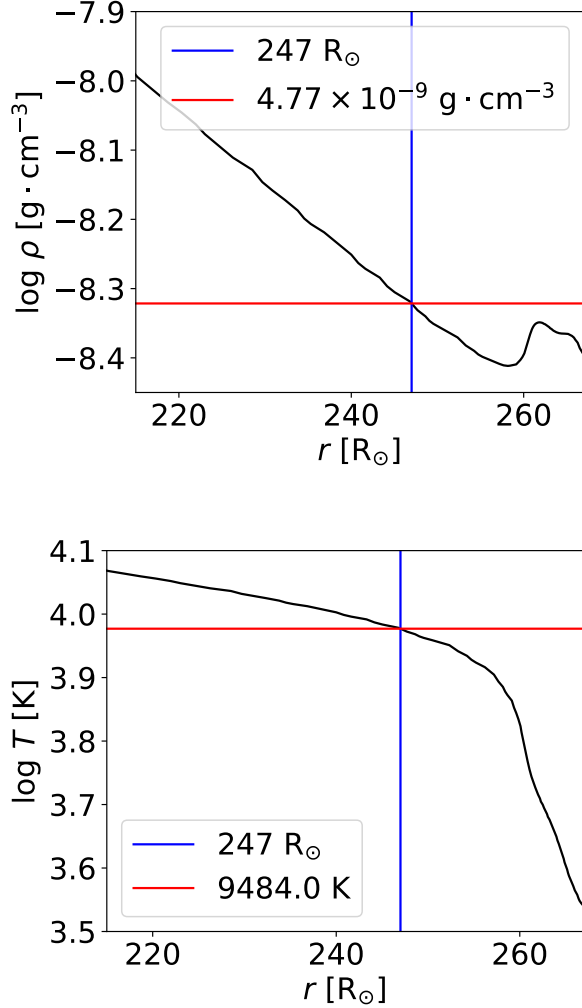


Figure 3. The zoomed in density and temperature profiles of the primary star produced by MESA. The piston position is placed at $R = 247R_{\odot}$.

mass-loss of the AGB star is lower. In this work, we adopt the AGB star with high mass-loss rate therefore we set the amplitude as $9\text{km}\cdot\text{s}^{-1}$.

The AGB stars in all four binary models are not spinning in the lab frame. That means the AGB star is counter-rotating in the co-rotating frame. The reason for setting non-spinning AGB star is twofold:

1. Complete tidal spin-orbit coupling state of an AGB star with its orbital rotation is not warranted, and the degree of that coupling is unknown. [Saladino et al. \(2019\)](#) analyzed the spin-orbit coupling and found that for $d \in [4 - 6]\text{AU}$, the AGB star is spinning at 95% of the orbital angular frequency. The AGB star they analyzed has a radius of $330R_{\odot}$ and 33% larger than the bound-

ary of the AGB star ($247R_{\odot}$) we use. Since we have similar binary separation, the spinning rate of our AGB star should be smaller.

2. The single AGB star model we tested is a non-spinning one. We would have to test and verify many more single star models to justify the binary simulations with a spinning AGB star.

By setting the spin of the AGB star to be zero, we are underestimating the initial angular momentum in the outflow. We now show that the underestimation is not big compared to the orbital angular momentum. The z-component of the specific angular momentum in a thin shell of a sphere can be calculated by

$$j_z = \frac{2}{3}\omega R^2, \quad (28)$$

where $\omega = \Omega_b$ means the co-rotating state and $R = 247R_{\odot}$ is the radius of the piston layer. The orbital specific angular momentum at $d/3$ (the distance of the AGB star's center to the center of mass) is

$$j_p = \Omega_b d^2 / 9. \quad (29)$$

In our four binary simulations, the maximum ratio of j_z/j_p is 0.27. In a not fully co-rotating case, the ratio is smaller.

5.2. Secondary star

The secondary star is modeled as a point gravitational source. While it does not interact hydrodynamically, it is given the ability to remove such material in its vicinity that has become bound to it. The mass of the removed material is added to the point particle representing the secondary ([Krumholz et al. 2004](#)). The point particle does not have the energy or spin angular momentum, therefore, the energy and angular momentum in the removed material is simply removed from the simulation. We define the 'vicinity' of the secondary to be $r_{\text{acc}} = 0.2$ AU or 8 finest cells in all of our simulations. We use spline softening ([Federrath et al. 2010](#)) to soft the gravitational force of the secondary within $r_{\text{soft}} = 0.1$ AU.

6. RESULTS

6.1. Single star

We first present the results of the single AGB star with the adopted physics and boundary conditions. Figure 4 shows the time-dependent mass-loss rate and piston's radial velocity, the wind's radial velocity profile and escape velocity and the time-dependent ρ and T measured at a distance $r = 2.75$ AU from the center of the single AGB star. The phase difference between the mass-loss

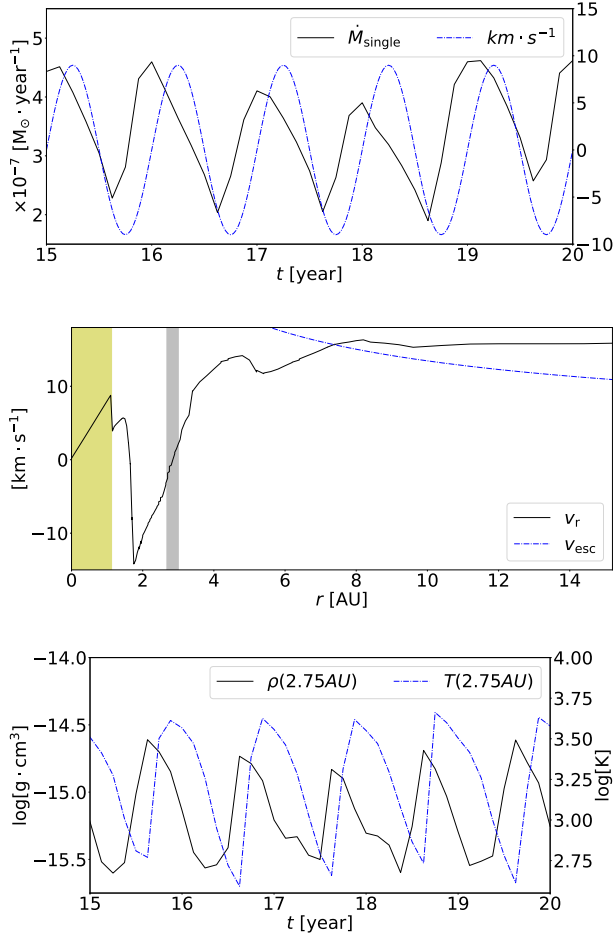


Figure 4. From the top to bottom: the mass-loss rate of the single AGB star model and the piston’s radial velocity, the radial velocity profile of the wind of the x-axis and the escape speed, and the time-dependent gas density and gas temperature at $r = 2.75$ AU on the x-axis. The AGB star is covered with the yellow band. The dust forming region is highlighted with the gray band in the middle panel.

rate and the piston’s radial velocity is irrelevant because it simply depends on the sampling shell of the mass flux.

We find that the mass-loss rate varies along with the phase of pulsation. The difference in phase is related to the radius of the flux sampling shell. We evaluate the mass flux at $r_p = 10$ AU. The average mass-loss rate is $\dot{M}_{\text{single}} = 3.45 \times 10^{-7} M_{\odot} \cdot \text{year}^{-1}$. Due to falling back material and continuing pulsations, the gas between the dust formation region and the piston boundary is constantly shocked, which can be seen in the middle panel. The wind’s velocity profile approaches a constant value at large distances. This terminal velocity of the AGB wind is $v_{\infty} \approx 15.8 \text{ km} \cdot \text{s}^{-1}$. A good summary of the relation of the luminosity, effective temperature, and mass-loss rate versus the wind terminal speed of M-

type AGB stars can be found in Figure 18 in Höfner & Olofsson (2018). The mass-loss rate in our model is within the range of the observed mass-loss rate of $10^{-7} - 10^{-5} M_{\odot} \cdot \text{year}^{-1}$. v_{∞} maybe a bit high. According to Höfner & Olofsson (2018), a more reasonable wind terminal speed should be between $7 \text{ km} \cdot \text{s}^{-1}$ and $13 \text{ km} \cdot \text{s}^{-1}$. However, this fact would not adversely affect the conclusions of this work as an AGB binary with a slow AGB wind is more likely to form a circumbinary disk (see Section 6.2).

Phase differences of different quantities may play important roles in the mass-loss rate. Liljegren et al. (2016) studied the impact of the phase difference between the pulsation and luminosity. They find that different phase shifts could lead to drastically different mass-loss rates. In our model, there is no phase difference in ρ and T in the piston. However, the phase between $\rho(2.75 \text{ AU})$ and $T(2.75 \text{ AU})$ differs by about 25% of the pulsation period. Because we do not consider the energy transfer by radiation, such a phase shift is mainly caused by cooling and shocks. According to criterion 3 of dust formation in Section 2.2, we can see from the third panel that there are moments when the dust is destroyed at the radius we probe. However, we need to be careful about the temperature variation here because, in reality, H_2 dissociation may absorb a large amount of energy, and the temperature may not rise to the point that sublimates the dust. A full consideration of the EoS is necessary to an accurate model of the dust formation and AGB wind.

6.2. Morphology of the outflow

We present the morphology of the outflows in four binary simulations in Figure 5. The AGB star is in the lower half of each plot. We can distinguish two large-scale patterns of outflow structure: the circumbinary disk and the spiral outflow. Specifically, circumbinary disks are found in the two simulations with the smallest separations, while spiral outflows are found in the two widest AGB binaries. Chen et al. (2017) also sees these two morphologies.

At a smaller scale, we can distinguish between the appearance or not of the accretion disk around the secondary. Specifically, there is no accretion disk in the simulation with $d = 6.0$ AU, while there are thin accretion disks in all the other cases (See Figure 6). In exploring the cause of the absence of an accretion disk in the $d = 6.0$ AU simulation, we tested a $d = 6.0$ AU simulation just without accretion. It turns out that a disk appears around the secondary (see Appendix B). We think the absence of the accretion disk in the $d = 6.0$ AU simulation when the accretion turned on maybe a

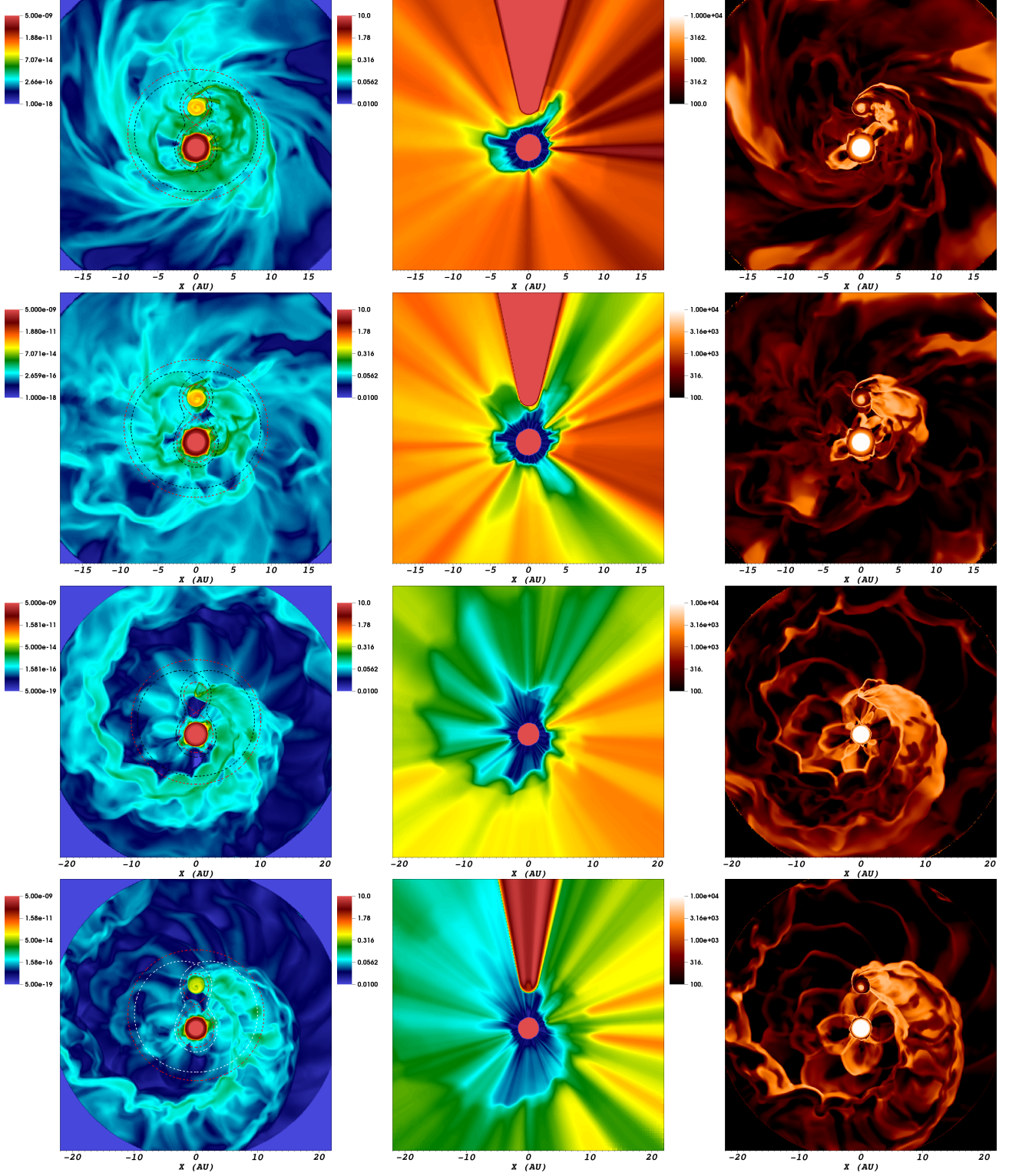


Figure 5. The snapshots for four binaries simulations in XY plane at $Z = 0$ for ρ [$\text{g}\cdot\text{cm}^{-3}$], τ , and T [K] (from the left to right). From the top to the bottom we show the simulations with $d = 5.4, 5.7, 6.0$ and 6.6 AU, respectively. The snapshots are provided at 10.32, 13.77, 7.46, and 9.13 orbits, respectively. In density plots we also show L_1 potential with red dashed lines and L_2 potential with black or white dashed lines, depending on the background.

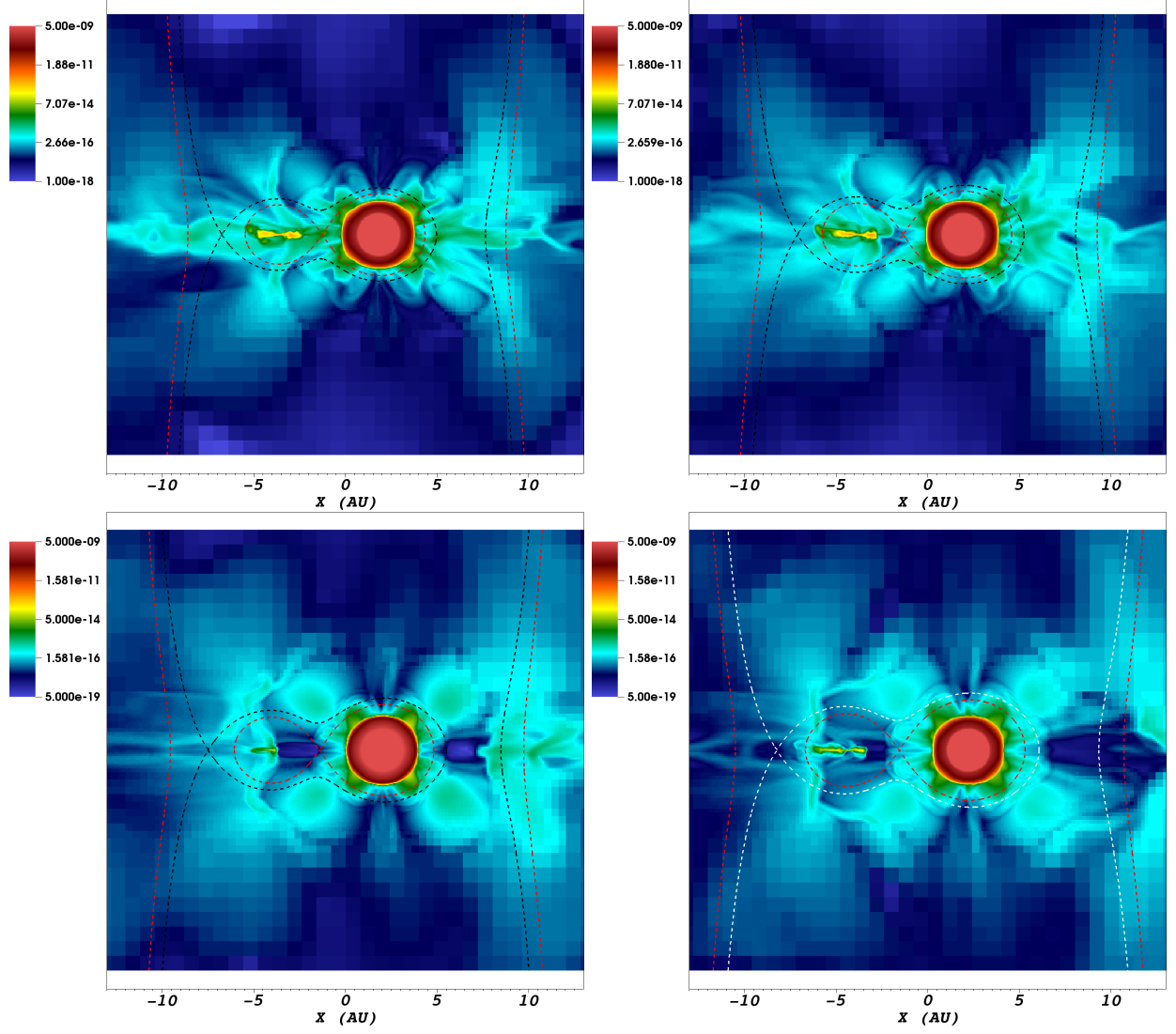


Figure 6. The snapshots for four binaries simulations in XZ plane at $Y = 0$ for ρ [$\text{g}\cdot\text{cm}^{-3}$]. The figure shows the results from simulations with $d = 5.4, 5.7, 6.0$ and 6.6 AU from the top left panel to the bottom right panel, respectively. Correspondingly, the snapshots are provided at 10.32, 13.77, 7.46, and 9.13 orbits. We also show L_1 potential with red dashed lines and L_2 potential with black or white dashed lines, depending on the background.

result of some interplay between the Cartesian mesh and accretion algorithm. At the edges of the accretion disks, the bow shocks are formed (see temperature plots in Figure 5, the shocked material has a higher temperature).

We find that, on average, the optical thickness decreases as the binary separation increases (see Figure 5). Each pulsation of the AGB star results in a formation of new clumps in the equator. The set of clumps increases the optical depth irregularly. The accretion disks cast sharp shadows, blocking the radiation from the AGB star.

To qualitatively understand the transition from the spiral outflow structure to the formation of circumbinary disk, we can first consider a spiral outflow that has a finite opacity and a very low density. In this case, the outflow experiences almost the same ratio of $a_{\text{rad}}/a_{\text{AGB}}$ where a_{AGB} is the gravitational acceleration from the AGB star. The outflow can escape the binary system if a_{rad} (or the luminosity of the AGB star) is large enough. If we hold the luminosity of the AGB star constant and increase the density in the spiral outflow, the optical thickness increases, and the value of a_{rad} acting on the outflow material decreases. When the optical thickness increases so fast that a_{rad} near the secondary orbit becomes too small to keep the total acceleration positive, the material in the outflow is less likely to escape from the binary system and a circumbinary disk forms. The closer the binary, the more material will be gravitationally focused towards the equatorial plane, and hence a circumbinary disk is more likely to form. In addition, the accretion disk blocks radiation from the primary star. When the material passes behind the disk's shadow, the amount of acceleration it can receive from radiation drops to zero, and the material is more likely to experience a fallback towards binary. In Section 6.1, we find that the AGB wind model we adopted has a high wind speed compared to observations and some theoretical models. A high-speed AGB wind is actually less likely to be captured or deflected by the secondary. Nevertheless, our simulations still show that circumbinary disks form. Our model and results suggest that circumbinary disks may form with larger binary separation, and they may be more common in AGB binaries.

In this work, we do not consider the eccentricity pumping and any non-circular motion because the (undetermined) numerical viscosity in our model prevents us from accurately modeling resonances. The interaction between a circumbinary disk and the binary may be one of the sources of the eccentricity (Artymowicz & Lubow 1994).

6.3. Mass transfer efficiency

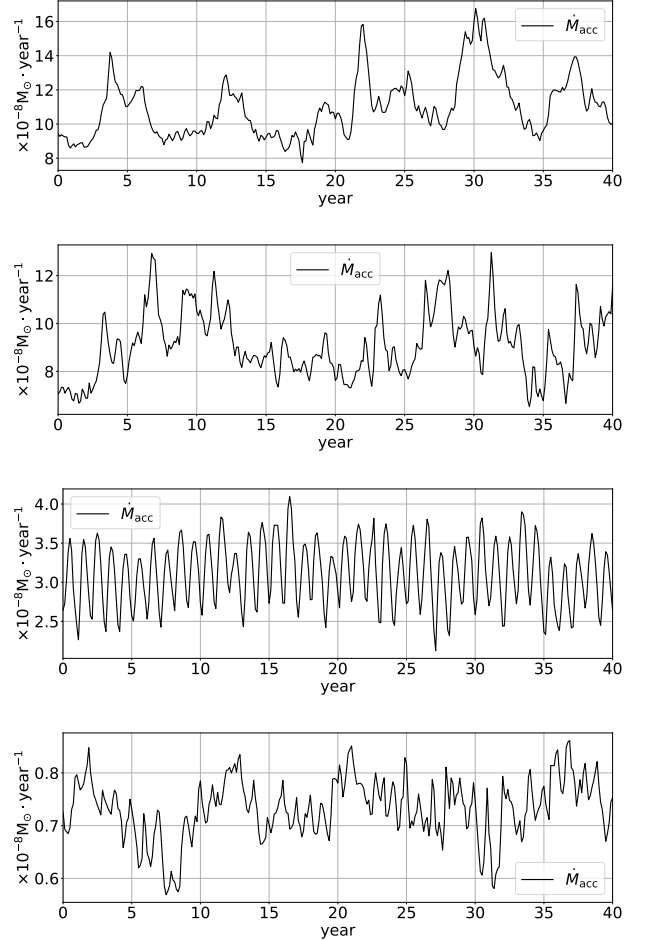


Figure 7. \dot{M}_{acc} in the simulations with $d = 5.4$ AU, $d = 5.7$ AU, $d = 6.0$ AU, and $d = 6.6$ AU from the top to bottom. The time interval over which the accretion rate is averaged is 0.125 year.

We define the mass transfer efficiency as

$$\beta = \dot{M}_{\text{acc}}/\dot{M}_{\text{p}}, \quad (30)$$

where \dot{M}_{acc} and \dot{M}_{p} are the accretion rate of the secondary and the mass-loss rate of the primary. We show the \dot{M}_{acc} during the final 40 years of simulations in all models in Figure 7.

We find that the accretion rate varies, and the smaller the distance between the stars, the larger and more irregular is the variation - \dot{M}_{acc} changes by a factor of 2 for $d = 5.4$ AU but only by 30% for $d = 6.6$ AU simulations. We may attribute the irregularity of the accretion rate to the following two reasons.

1. The resolution around the secondary may be too low. We use $r_{\text{soft}} = 0.1$ AU which corresponds to 4 finest cells in our simulation. Low resolution in grid-based hydrodynamics can result in a high and

d	\dot{M}_p	\dot{M}_{acc}	\dot{M}_{flux}	β	r_{half}/r_{L1}	\dot{M}_{BHL}	β_{BHL}	$\frac{v_\infty}{v_{orbit}}$	morpho	mechanism
[AU]	[$M_\odot \cdot \text{year}^{-1}$]	[$M_\odot \cdot \text{year}^{-1}$]	[$M_\odot \cdot \text{year}^{-1}$]	[%]		[$M_\odot \cdot \text{year}^{-1}$]	[%]			
5.4	3.48×10^{-7}	1.08×10^{-7}	2.40×10^{-7}	31	0.921	1.37×10^{-8}	3.96	1.00	CB	WRLOF
5.7	3.49×10^{-7}	9.09×10^{-8}	2.58×10^{-7}	26	0.857	1.28×10^{-8}	3.70	1.02	CB	WRLOF
6.0	4.31×10^{-7}	3.11×10^{-8}	4.00×10^{-7}	7.2	0.814	1.20×10^{-8}	3.47	1.05	SO	WRLOF
6.6	4.04×10^{-7}	7.37×10^{-9}	3.97×10^{-7}	1.8	0.740	1.06×10^{-8}	3.06	1.10	SO	BHL

Table 2. Average mass-loss rate, accretion rate, and mass flux through the sampling shell of the four simulations. β is the mass transfer efficiency. The results of the BHL accretion scenario are also calculated. v_∞/v_{orbit} is calculated as a reference. Morpho refers to the outflow morphology. CB and SO are short for circumbinary disk and spiral outflow which can be seen in Figure 5. Mechanism refers to the mass transfer mechanism, in our simulations, it is either the WRLOF or the BHL accretion.

not smooth numerical viscosity. This numerical viscosity in multidimensional hydrodynamic simulations could be larger than the physical viscosity. In accretion disk, a higher viscosity could lead to a higher accretion rate (Frank et al. 2002). Also, the small number of cells of the accretion zone around the secondary may contribute to the irregularity in the accretion (Krumholz et al. 2004).

2. The accretion algorithm is well tested in the BHL accretion scenario (Krumholz et al. 2004) but is not examined for accreting from an accretion disk. The direct interaction between an accreting particle and the disk around it may be intermittent because a sudden removal of some material at the center of a disk may create waves. The waves may affect the dynamics of the outer disk and create more waves. Additionally, we use cooling to remove energy inside the disk. The cooled gas is more likely to be accreted according to the accretion algorithm. However, the cooling rate depends on the density and velocity and is highly nonlinear. We anticipate that sometimes the cooling makes a chunk of gas to be less energetic and accreted.

The accretion rate of the two wide binaries is more regular. The pulsation period of the AGB star is 1 year, and we find that the accretion rate oscillates at a roughly same period. In Equation 30, \dot{M}_p is the sum of the mass flux \dot{M}_{flux} that leaves the binary system and \dot{M}_{acc} . We find average \dot{M}_{flux} by summing the mass flux through a spherical shell with $r_{shell} = 10$ AU and centered at the origin. We then average \dot{M}_{flux} over 40 years, see Table 2. At the same time we can find what accretion rate can be predicted by the analytic BHL accretion model

$$\dot{M}_{BHL} = \frac{G^2 m_s^2 \dot{M}_{single}}{v_\infty (v_{orbit}^2 + v_\infty^2)^{3/2} d^2}, \quad (31)$$

Here $v_{orbit} = \Omega_b d$ is the relative speed between the two orbiting objects. and v_∞ is velocity of wind at infinity. Saladino et al. (2018) multiplied the RHS of Equation 31 by an efficiency parameter α_{BHL} which may vary from

0.8 to 1.5. This parameter is mainly empirical so we do not study which value is more appropriate for which AGB binary model. Readers can multiply β_{BHL} in Table 2 by a factor to get the corresponding range.

To find what the analytic BHL accretion would predict for our system, we adopt that the AGB star loses mass at the constant rate of \dot{M}_{single} and use a constant radial velocity of $v_\infty = 15.8 \text{ km} \cdot \text{s}^{-1}$ which is the terminal velocity of the AGB wind. Equation 31 is usually the upper limit of the BHL accretion rate as in its derivation it is assumed that in a parallel flow, every particle at a large distance with kinetic energy smaller than the absolute value of the gravitational energy at its closest encounter to be accreted. The mass transfer efficiency of the BHL accretion can be found as

$$\beta_{BHL} = \frac{\dot{M}_{BHL}}{\dot{M}_{single}} = \frac{G^2 m_s^2}{v_\infty (v_{orbit}^2 + v_\infty^2)^{3/2} d^2}. \quad (32)$$

We can see from Table 2 that only the simulation with $d = 6.6$ AU has \dot{M}_{acc} and β smaller than the BHL model. The simulation with $d = 6$ AU has \dot{M}_{acc} and β larger than the BHL model. At the same time we find that this simulation also exhibits a spiral outflow structure. This may suggest that WRLOF is taking place and the radiation pressure is still large enough to push away the material.

The two wide AGB binaries exhibit spiral outflow and have a higher mass-loss rate as compared to the two closer ones with circumbinary disks. It is because the circumbinary disk confines some of the gas in the equatorial region and the gas may fall back to the AGB star.

It has been argued that v_∞/v_{orbit} is the key parameter of the mass transfer efficiency, and the orbital evolution of a binary with an AGB star can be predicted by this parameter (Saladino et al. 2018). In our four AGB binary simulations, v_∞/v_{orbit} does not change much. However, the mass transfer efficiency changes drastically. The change in mass transfer efficiency seems to be closely related to the formation of the circumbinary disk. The formation of the circumbinary disk is related to the increase of the optical depth in the equatorial re-

gion (see Section 6.2). The formation of a circumbinary disk in close AGB binaries questions the applicability of the simplified mass transfer models.

6.4. Angular distribution of the outflow

The secondary deflects the outflow from the primary to the equator, making the shape of the outflow more bipolar (see also [Chen et al. 2017](#)). To quantitatively demonstrate that the secondary focuses the outflow onto the equatorial plane, we split the simulation domain into six bins in the polar angle, where each bin extends for 30° . We again evaluate the mass flux at 10AU from the origin. We find the time average mass of the outflow through each of the bins. We define the fraction of mass of the outflow in each bin as

$$f_i = \dot{M}_i / \dot{M}_p, \quad (33)$$

where \dot{M}_i is the mass of the outflow through the i th bin. Values of f_i are provided in Table 3.

Since the secondary is located at the equator, we distribute the accreted mass of the secondary among the two bins in the equatorial region evenly. We find that the outflow of our single star is slightly not isotropic, albeit it is quite symmetric with respect to the polar angle. Its outflow is exceeding a fully isotropic case by about 20% in the $30 - 60^\circ$ region. The Cartesian mesh probably causes anisotropy.

From Table 3, one can see that the outflow is strongly concentrated in the equatorial region in all four binary simulations. Let us compare the equatorial bin f_3 for all four binary simulations. If we compare the two close binaries with the circumbinary disk, the closer one (5.4AU) has a greater f_3 . Similarly, if we compare the two wide binaries with spiral outflow, the closer one (6.0AU) has a greater f_3 . If a circumbinary disk is present, some material in the equatorial region may fall back to the AGB star, which can be inferred in the total mass-loss rate \dot{M}_p in Table 2.

6.5. Orbital stability

In Section 3.1, we adopted that the orbit of the binary is circular and does not change. In nature, the binary orbit would change due to the loss of the angular momentum. Here we evaluate the potential rate of the orbital change and check posteriorly if our assumption in Section 3.1 is justified.

The total angular momentum J of the binary system and the specific angular momentum of the binary system

j are

$$J = m_p m_s \sqrt{\frac{Gd}{m_p + m_s}}, \quad (34)$$

$$j = m_p m_s \sqrt{\frac{Gd}{(m_p + m_s)^3}}. \quad (35)$$

It does not include any stellar spin as in our simulations stars were considered to not rotate. We define γ_{am} to be the multiple of the specific angular momentum in the outflow in terms of the specific angular momentum of the binary system

$$j_{\text{outflow}} = \gamma_{\text{am}} j. \quad (36)$$

It is a measure of the efficiency of angular momentum loss. Making use of γ_{am} , β , and the mass ratio $q = m_p/m_s$, the rate of change of the binary separation can be expressed by

$$\frac{\dot{d}}{d} = 2 \frac{\dot{M}_p}{m_p} \left(1 - \beta q - (1 - \beta) \left(\gamma_{\text{am}} + \frac{1}{2} \right) \frac{q}{1 + q} \right). \quad (37)$$

We have calculated \dot{M}_p and β of each binary simulation in Section 6.3. The only unknown is γ_{am} . We get γ_{am} from the binary simulations by evaluating the average γ_{am} through a spherical shell whose radius is $1.3d$ and center is at the center of mass of the binary. By setting the sampling radius at $1.3d$, we probably underestimate the angular momentum loss from the binary because the escaping gas can still gain angular momentum as it goes beyond $1.3d$ ([Lin 1977](#); [Saladino et al. 2018](#)). However, the angular momentum conservation becomes worse in our code as the radius goes large ([Chen et al. 2018](#)). We prefer not to incur too much uncertainty, so we set the sampling shell small. In the absence of the spin angular momentum and $q = 2$, when $\gamma \approx 0.5$, the gas emitted from the AGB star does not gain any angular momentum, when $\gamma \approx 2$, the escaping gas has a specific angular momentum that equals the secondary. Table 4 lists γ_{am} of each of our binary simulation and the potential rate of change of the orbit.

From Table 4, we can infer that the binary separation in our four binary simulations should not change more than 5×10^{-4} AU. Therefore, our assumption in Section 3.1 is reasonable. On the other hand, if the binary separation change rate is kept constant for 10^6 years, the decrease in binary separation of the two close binary is non-negligible. Considering that we have ignored the spin-orbit coupling of the binary and we set a small sampling shell to get γ_{am} , we are underestimating the orbital angular momentum loss. The actual orbital shrinkage should be higher. As the binary separation decreases, the WRLOF may become more similar to the RLOF.

model name	f_1	f_2	f_3	f_4	f_5	f_6
	[0, 30°]	[30°, 60°]	[60°, 90°]	[90°, 120°]	[120°, 150°]	[150°, 180°]
isotropic	6.70×10^{-2}	1.83×10^{-1}	2.50×10^{-1}	2.50×10^{-1}	1.83×10^{-1}	6.70×10^{-2}
single	5.23×10^{-2}	2.19×10^{-1}	2.31×10^{-1}	2.28×10^{-1}	2.18×10^{-1}	5.26×10^{-2}
5.4AU	1.29×10^{-2}	1.33×10^{-1}	3.62×10^{-1}	3.54×10^{-1}	1.27×10^{-1}	1.18×10^{-2}
5.7AU	1.43×10^{-2}	1.48×10^{-1}	3.42×10^{-1}	3.36×10^{-1}	1.47×10^{-1}	1.40×10^{-2}
6.0AU	1.38×10^{-2}	1.18×10^{-1}	3.76×10^{-1}	3.67×10^{-1}	1.12×10^{-1}	1.33×10^{-2}
6.6AU	1.83×10^{-2}	1.46×10^{-1}	3.36×10^{-1}	3.44×10^{-1}	1.38×10^{-1}	1.77×10^{-2}

Table 3. The fraction of mass of outflow through binned polar angular range. The second row list the polar angle range of each bin in degree. 0° corresponds to the positive z direction. The third row presents the result if the flux is isotropic. The fourth row shows the result from the single star from Section 6.1. The results of the four binary simulations are listed from row 4 to row 8.

d	γ_{am}	$\delta\gamma_{\text{am}}$	\dot{d}/d	Δd
[AU]		[%]	[year ⁻¹]	[AU]
5.4	0.955	91.0	-1.98×10^{-7}	-1.07×10^0
5.7	0.946	89.2	-1.60×10^{-7}	-9.11×10^{-1}
6.0	0.879	75.8	2.52×10^{-9}	1.51×10^{-2}
6.6	0.815	63.0	8.16×10^{-8}	5.38×10^{-1}

Table 4. The measured γ_{am} of the four binary models and relative rate of the change of the binary separation. $\delta\gamma_{\text{am}} = ((\gamma_{\text{am}} - 0.5)/0.5) \times 100\%$ is the percentile difference of the specific angular momentum of the outflow compared to the specific angular momentum of the AGB star. The fourth column show the potential change in 10⁶ years if the binary separation change rate is kept constant.

7. CONCLUSIONS AND DISCUSSIONS

In this paper, we carry out 3D radiation hydrodynamic simulations of AGB binaries. We use ray-tracing radiation transfer to resolve the optical depth in the azimuthal and polar directions. We take into account dust which can be destroyed by shocks, a high temperature close to an LTE environment, and if radiation from the AGB star can sublimate the small dust grains (see Section 3.2 for detail). We calculate the cooling strength on H₂, H, and H⁺; their number densities are found by solving the Saha equation (Chen et al. 2019). We model the AGB star as an inner boundary condition that has sinusoidally varying radial velocity (Bowen 1988). We use MESA to obtain the temperature and density that determine the boundary conditions of our piston model.

The single star model presented in Section 6.1 has an average mass-loss rate of $3.45 \times 10^{-7} \text{M}_{\odot} \cdot \text{year}^{-1}$ and a terminal wind speed of $15.8 \text{km} \cdot \text{s}^{-1}$. We find that the mass-loss rate is very reasonable for an M-type AGB star with an effective temperature of 2874K and a luminosity of $4384 L_{\odot}$ (Höfner & Olofsson 2018). Observations show that the terminal wind speed should be $7 - 13 \text{km} \cdot \text{s}^{-1}$ (Höfner & Olofsson 2018). However, we argued that this difference would not adversely affect our conclusion. On the contrary, lower terminal wind

speed may be captured or deflected by the secondary more easily. In the case of low wind speed, a circumbinary disk would form with a larger binary separation (see Section 6.2 for detail).

We find that the accretion rate increases when the binary separation decreases (see Table 2). The mass transfer efficiency may increase dramatically to 31% when circumbinary disk forms. Such a mass transfer efficiency is about eight times more than what the analytical BHL accretion rate predicts. The presence of a circumbinary disk imposes severe challenges to the simplified mass transfer mechanisms. It enlarges the domain of dependence of the secondary to the whole equatorial region. The circumbinary disk may also exert a torque on the binary and change the eccentricity of the binary system (Artymowicz & Lubow 1994; Dermine et al. 2013; Moody et al. 2019). The eccentricity problem has been heavily studied by the proto-planetary disk community, and similar conditions may apply here (Ragusa et al. 2018). The formation of a circumbinary disk is a result of the focused fluids in the equatorial plane by the secondary (Section 6.4). The focused fluids increase the optical depth in the equatorial plane; thus, the radiation pressure on the fluids decreases. The balance between the radiation pressure and the gravity will be tilted toward the gravity when the optical depth becomes larger than a critical value, and some of the gas may fall back. We find it interesting that the 6AU binary has a mass transfer rate more than two times higher than the BHL accretion without a circumbinary disk. This result exemplifies the difference in mass transfer efficiency between the WRLOF and BHL accretion.

The accretion rates in the two closest AGB binaries are irregular. We outlined two possible reasons for the irregularity in Section 6.3. It may be worthwhile to increase the resolution and allow a subsonic atmosphere (or envelope) to build up around the secondary in future researches. The atmosphere can provide a subsonic region that may smooth out the supersonic flow that falls

onto the secondary. The particle can accrete mass from the atmosphere when the atmosphere becomes Jeans unstable (Jeans 1902; Federrath et al. 2010). It is also natural to model proper feedback, i.e., radiative cooling, from the secondary when an atmosphere presents. In our current model, we have not taken radiative feedback from the accretor and the radiation transfer in the accretion disk into consideration. In a real circumstance, the accretion disk will become optically thick when the density of the disk becomes high enough. The transition from the optically thin to the optically thick state may incur different accretion modes. A better understanding of the accretion rate may be achieved by modeling the transition correctly.

The two closest binaries have dusty circumbinary disks, which may resemble the situation AR Puppis (ErteI et al. 2019). The two widest binaries have spiral structure outflows. Such structure resembles many post-AGB binaries with wide binary separations or planetary nebulae (Edgar et al. 2008; Maercker et al. 2012; Ramstedt et al. 2017; Sabach & Soker 2018; Kim et al. 2019).

In Section 6.5, we discussed the orbital dynamics of the AGB binaries in our simulations. We confirmed that it is reasonable to ignore the orbital evolution in our simulations. We also find that the two closest AGB binaries may experience an orbital shrinkage, where the binary with the initial separation of 5.4AU has the fastest orbital separation decreasing rate. Since we did not consider the tidal spin-orbit coupling and excluded the contribution of angular momentum transfer beyond 1.3 binary separation from the center of mass in the calculation of γ_{am} , we are underestimating the orbital angular momentum loss in close binaries. The decrease of the binary separation in the two close binaries should be faster than what we estimated. The binary with 5.4AU initial separation may become RLOF as it evolves.

When there is no circumbinary disk, the longest timescale in AGB binaries is typically the binary’s orbit. When a circumbinary disk presents, the overall conditions (density, chemistry, and timescale) become similar to a proto-planetary disk. The temperature in the circumbinary disk may change a lot because of the

shocks and radiation from the AGB star. The material in the equatorial region may stay close to the binary for several or more orbits. The dense environment ($10^{-15} - 10^{-14} \text{g.cm}^{-3}$ in the middle plane near the binary orbit) in the circumbinary disks can also foster dust growth. Large dust grains may process photons with a wavelength longer than the K band. If multiple scattering by the dust becomes essential, a more sophisticated non-gray radiative transfer model is in need. In our simulations, we find that the optical depth as calculated along the line of sight from the AGB star is typically less than 10 (except for the accretion disk). Monte Carlo radiative transfer would be an efficient way to model the radiation-hydrodynamics in the circumbinary disk.

In summary, the mass transfer efficiency β and angular momentum loss efficiency γ_{am} are two important quantities but with large uncertainty in AGB binaries. They hugely affect the orbital and stellar evolution of the binaries. In this work, we derived β and γ_{am} from 3D radiation-hydrodynamic simulations. We discover a huge discrepancy (up to eight times) in β by comparing our simulations with simple mass transfer models. The discrepancy is closely related to the presence of the circumbinary disks.

ACKNOWLEDGMENTS

We thank Craig Heinke, Rodrigo Fernandez, Xuening Bai, Falk Herwig, Pavel Denisenkov, Nami Mowlavi, and Ue-Li Pen for inspirational discussions. ZC is grateful to the CITA National Postdoctoral Fellowship for financial support. N.I. acknowledges support from CRC program and funding from NSERC Discovery. This research was enabled by the use of computing resources provided by Compute/Calcul Canada, and was supported in part by the National Science Foundation under Grant No. NSF PHY-1748958.

Software: AstroBEAR (Carroll-Nellenback et al. 2013), matplotlib (Hunter 2007), MESA v10398 (Paxton et al. 2011, 2013, 2015, 2018), Visit 3.0.1 (Childs et al. 2012).

REFERENCES

- Abate, C., Pols, O. R., Izzard, R. G., & Karakas, A. I. 2015, *A&A*, 581, A22, doi: [10.1051/0004-6361/201525876](https://doi.org/10.1051/0004-6361/201525876)
- Abate, C., Pols, O. R., Izzard, R. G., Mohamed, S. S., & de Mink, S. E. 2013, *A&A*, 552, A26, doi: [10.1051/0004-6361/201220007](https://doi.org/10.1051/0004-6361/201220007)
- Artymowicz, P., & Lubow, S. H. 1994, *ApJ*, 421, 651, doi: [10.1086/173679](https://doi.org/10.1086/173679)
- Bidelman, W. P., & Keenan, P. C. 1951, *ApJ*, 114, 473, doi: [10.1086/145488](https://doi.org/10.1086/145488)
- Bladh, S., Höfner, S., Nowotny, W., Aringer, B., & Eriksson, K. 2013, *A&A*, 553, A20, doi: [10.1051/0004-6361/201220590](https://doi.org/10.1051/0004-6361/201220590)
- Bondi, H., & Hoyle, F. 1944, *MNRAS*, 104, 273, doi: [10.1093/mnras/104.5.273](https://doi.org/10.1093/mnras/104.5.273)

- Boulanger, J., Clementel, N., van Marle, A. J., Decin, L., & de Koter, A. 2019a, *MNRAS*, 482, 5052, doi: [10.1093/mnras/sty2560](https://doi.org/10.1093/mnras/sty2560)
- Boulanger, J., Gobrecht, D., Decin, L., de Koter, A., & Yates, J. 2019b, arXiv e-prints, arXiv:1908.09633. <https://arxiv.org/abs/1908.09633>
- Bowen, G. H. 1988, *ApJ*, 329, 299, doi: [10.1086/166378](https://doi.org/10.1086/166378)
- Carroll-Nellenback, J. J., Shroyer, B., Frank, A., & Ding, C. 2013, *Journal of Computational Physics*, 236, 461, doi: [10.1016/j.jcp.2012.10.004](https://doi.org/10.1016/j.jcp.2012.10.004)
- Cen, R. 1992, *ApJS*, 78, 341, doi: [10.1086/191630](https://doi.org/10.1086/191630)
- Chen, Z., Blackman, E. G., Nordhaus, J., Frank, A., & Carroll-Nellenback, J. 2018, *MNRAS*, 473, 747, doi: [10.1093/mnras/stx2335](https://doi.org/10.1093/mnras/stx2335)
- Chen, Z., Coleman, M. S. B., Blackman, E. G., & Frank, A. 2019, *Journal of Computational Physics*, 388, 490, doi: [10.1016/j.jcp.2019.03.016](https://doi.org/10.1016/j.jcp.2019.03.016)
- Chen, Z., Frank, A., Blackman, E. G., Nordhaus, J., & Carroll-Nellenback, J. 2017, *MNRAS*, 468, 4465, doi: [10.1093/mnras/stx680](https://doi.org/10.1093/mnras/stx680)
- Childs, H., Brugger, E., Whitlock, B., et al. 2012, in *High Performance Visualization—Enabling Extreme-Scale Scientific Insight*, 357–372
- Colella, P. 1990, *Journal of Computational Physics*, 87, 171, doi: [10.1016/0021-9991\(90\)90233-Q](https://doi.org/10.1016/0021-9991(90)90233-Q)
- Dahn, C. C., Liebert, J., Kron, R. G., Spinrad, H., & Hintzen, P. M. 1977, *ApJ*, 216, 757, doi: [10.1086/155518](https://doi.org/10.1086/155518)
- de Val-Borro, M., Karovska, M., Sasselov, D. D., & Stone, J. M. 2017, *MNRAS*, 468, 3408, doi: [10.1093/mnras/stx684](https://doi.org/10.1093/mnras/stx684)
- Dermine, T., Izzard, R. G., Jorissen, A., & Van Winckel, H. 2013, *A&A*, 551, A50, doi: [10.1051/0004-6361/201219430](https://doi.org/10.1051/0004-6361/201219430)
- Dorschner, J., Begemann, B., Henning, T., Jaeger, C., & Mutschke, H. 1995, *A&A*, 300, 503
- Edgar, R. 2004, *NewAR*, 48, 843, doi: [10.1016/j.newar.2004.06.001](https://doi.org/10.1016/j.newar.2004.06.001)
- Edgar, R. G., Nordhaus, J., Blackman, E. G., & Frank, A. 2008, *ApJL*, 675, L101
- Ertel, S., Kamath, D., Hillen, M., et al. 2019, *AJ*, 157, 110, doi: [10.3847/1538-3881/aafe04](https://doi.org/10.3847/1538-3881/aafe04)
- Escorza, A., Karinkuzhi, D., Jorissen, A., et al. 2019, *A&A*, 626, A128, doi: [10.1051/0004-6361/201935390](https://doi.org/10.1051/0004-6361/201935390)
- Federrath, C., Banerjee, R., Clark, P. C., & Klessen, R. S. 2010, *ApJ*, 713, 269, doi: [10.1088/0004-637X/713/1/269](https://doi.org/10.1088/0004-637X/713/1/269)
- Frank, J., King, A., & Raine, D. J. 2002, *Accretion Power in Astrophysics: Third Edition*
- Freytag, B., & Höfner, S. 2008, *A&A*, 483, 571, doi: [10.1051/0004-6361:20078096](https://doi.org/10.1051/0004-6361:20078096)
- Freytag, B., Liljegren, S., & Höfner, S. 2017, *A&A*, 600, A137, doi: [10.1051/0004-6361/201629594](https://doi.org/10.1051/0004-6361/201629594)
- Gail, H. P., Keller, R., & Sedlmayr, E. 1984, *A&A*, 133, 320
- Gail, H. P., & Sedlmayr, E. 1985, *A&A*, 148, 183
- . 1986, *A&A*, 166, 225
- . 1988, *A&A*, 206, 153
- Gezer, I., Van Winckel, H., Manick, R., & Kamath, D. 2019, *MNRAS*, 488, 4033, doi: [10.1093/mnras/stz1967](https://doi.org/10.1093/mnras/stz1967)
- Giridhar, S., Rao, N. K., & Lambert, D. L. 1994, *ApJ*, 437, 476, doi: [10.1086/175011](https://doi.org/10.1086/175011)
- Helling, C., & Woitke, P. 2006, *A&A*, 455, 325, doi: [10.1051/0004-6361:20054598](https://doi.org/10.1051/0004-6361:20054598)
- Heney, L. G., & Greenstein, J. L. 1941, *ApJ*, 93, 70, doi: [10.1086/144246](https://doi.org/10.1086/144246)
- Hillen, M., Kluska, J., Le Bouquin, J. B., et al. 2016, *A&A*, 588, L1, doi: [10.1051/0004-6361/201628125](https://doi.org/10.1051/0004-6361/201628125)
- Höfner, S., & Freytag, B. 2019, *A&A*, 623, A158, doi: [10.1051/0004-6361/201834799](https://doi.org/10.1051/0004-6361/201834799)
- Höfner, S., & Olofsson, H. 2018, *A&A Rv*, 26, 1, doi: [10.1007/s00159-017-0106-5](https://doi.org/10.1007/s00159-017-0106-5)
- Homan, W., Richards, A., Decin, L., et al. 2017, *A&A*, 601, A5, doi: [10.1051/0004-6361/201630340](https://doi.org/10.1051/0004-6361/201630340)
- Hoyle, F., & Lyttleton, R. A. 1939, *Proceedings of the Cambridge Philosophical Society*, 35, 405, doi: [10.1017/S0305004100021150](https://doi.org/10.1017/S0305004100021150)
- Huarte-Espinosa, M., Carroll-Nellenback, J., Nordhaus, J., Frank, A., & Blackman, E. G. 2013, *MNRAS*, 433, 295, doi: [10.1093/mnras/stt725](https://doi.org/10.1093/mnras/stt725)
- Hunter, J. D. 2007, *Computing in Science & Engineering*, 9, 90, doi: [10.1109/MCSE.2007.55](https://doi.org/10.1109/MCSE.2007.55)
- Jaeger, C., Mutschke, H., Begemann, B., Dorschner, J., & Henning, T. 1994, *A&A*, 292, 641
- Jeans, J. H. 1902, *Philosophical Transactions of the Royal Society of London Series A*, 199, 1, doi: [10.1098/rsta.1902.0012](https://doi.org/10.1098/rsta.1902.0012)
- Jeong, K. S., Winters, J. M., Le Bertre, T., & Sedlmayr, E. 2003, *A&A*, 407, 191, doi: [10.1051/0004-6361:20030693](https://doi.org/10.1051/0004-6361:20030693)
- Jorissen, A., Van Eck, S., Van Winckel, H., et al. 2016, *A&A*, 586, A158, doi: [10.1051/0004-6361/201526992](https://doi.org/10.1051/0004-6361/201526992)
- Karambelkar, V. R., Adams, S. M., Whitelock, P. A., et al. 2019, *ApJ*, 877, 110, doi: [10.3847/1538-4357/ab1a41](https://doi.org/10.3847/1538-4357/ab1a41)
- Keenan, P. C. 1942, *ApJ*, 96, 101, doi: [10.1086/144435](https://doi.org/10.1086/144435)
- Kervella, P., Montargès, M., Lagadec, E., et al. 2015, *A&A*, 578, A77, doi: [10.1051/0004-6361/201526194](https://doi.org/10.1051/0004-6361/201526194)
- Khouri, T., Velilla-Prieto, L., De Beck, E., et al. 2019, *A&A*, 623, L1, doi: [10.1051/0004-6361/201935049](https://doi.org/10.1051/0004-6361/201935049)
- Kim, H., Liu, S.-Y., & Taam, R. E. 2019, *ApJS*, 243, 35, doi: [10.3847/1538-4365/ab297e](https://doi.org/10.3847/1538-4365/ab297e)
- Kobayashi, H., Kimura, H., Watanabe, S. i., Yamamoto, T., & Müller, S. 2011, *Earth, Planets, and Space*, 63, 1067, doi: [10.5047/eps.2011.03.012](https://doi.org/10.5047/eps.2011.03.012)

- Krumholz, M. R., McKee, C. F., & Klein, R. I. 2004, *ApJ*, 611, 399, doi: [10.1086/421935](https://doi.org/10.1086/421935)
- Lacy, J. H., Knacke, R., Geballe, T. R., & Tokunaga, A. T. 1994, *ApJL*, 428, L69, doi: [10.1086/187395](https://doi.org/10.1086/187395)
- Lamers, H. J. G. L. M., & Cassinelli, J. P. 1999, *Introduction to Stellar Winds*
- Liljegren, S., Höfner, S., Nowotny, W., & Eriksson, K. 2016, *A&A*, 589, A130, doi: [10.1051/0004-6361/201527885](https://doi.org/10.1051/0004-6361/201527885)
- Lin, D. N. C. 1977, *MNRAS*, 179, 265, doi: [10.1093/mnras/179.2.265](https://doi.org/10.1093/mnras/179.2.265)
- Liu, Z.-W., Stancliffe, R. J., Abate, C., & Matrozis, E. 2017, *ApJ*, 846, 117, doi: [10.3847/1538-4357/aa8622](https://doi.org/10.3847/1538-4357/aa8622)
- Maercker, M., Mohamed, S., Vlemmings, W. H. T., et al. 2012, *Nature*, 490, 232, doi: [10.1038/nature11511](https://doi.org/10.1038/nature11511)
- Manick, R., Van Winckel, H., Kamath, D., Hillen, M., & Escorza, A. 2017, *A&A*, 597, A129, doi: [10.1051/0004-6361/201629125](https://doi.org/10.1051/0004-6361/201629125)
- Mathis, J. S., Rumpl, W., & Nordsieck, K. H. 1977, *ApJ*, 217, 425, doi: [10.1086/155591](https://doi.org/10.1086/155591)
- Mätzler, C. 2002, *IAP Res. Rep.*, 8, 9
- McClure, R. D., & Woodsworth, A. W. 1990, *ApJ*, 352, 709, doi: [10.1086/168573](https://doi.org/10.1086/168573)
- Mohamed, S., & Podsiadlowski, P. 2012, *Baltic Astronomy*, 21, 88, doi: [10.1515/astro-2017-0362](https://doi.org/10.1515/astro-2017-0362)
- Moody, M. S. L., Shi, J.-M., & Stone, J. M. 2019, *ApJ*, 875, 66, doi: [10.3847/1538-4357/ab09ee](https://doi.org/10.3847/1538-4357/ab09ee)
- Mowlavi, N., Lecoœur-Taïbi, I., Lebzelter, T., et al. 2018, *A&A*, 618, A58, doi: [10.1051/0004-6361/201833366](https://doi.org/10.1051/0004-6361/201833366)
- Neufeld, D. A., & Kaufman, M. J. 1993, *ApJ*, 418, 263, doi: [10.1086/173388](https://doi.org/10.1086/173388)
- Oomen, G.-M., Van Winckel, H., Pols, O., & Nelemans, G. 2019, *A&A*, 629, A49, doi: [10.1051/0004-6361/201935853](https://doi.org/10.1051/0004-6361/201935853)
- Ortiz, R., & Guerrero, M. A. 2016, *MNRAS*, 461, 3036, doi: [10.1093/mnras/stw1547](https://doi.org/10.1093/mnras/stw1547)
- Paxton, B., Bildsten, L., Dotter, A., et al. 2011, *ApJS*, 192, 3, doi: [10.1088/0067-0049/192/1/3](https://doi.org/10.1088/0067-0049/192/1/3)
- Paxton, B., Cantiello, M., Arras, P., et al. 2013, *ApJS*, 208, 4, doi: [10.1088/0067-0049/208/1/4](https://doi.org/10.1088/0067-0049/208/1/4)
- Paxton, B., Marchant, P., Schwab, J., et al. 2015, *ApJS*, 220, 15, doi: [10.1088/0067-0049/220/1/15](https://doi.org/10.1088/0067-0049/220/1/15)
- Paxton, B., Schwab, J., Bauer, E. B., et al. 2018, *ApJS*, 234, 34, doi: [10.3847/1538-4365/aaa5a8](https://doi.org/10.3847/1538-4365/aaa5a8)
- Podsiadlowski, P., & Mohamed, S. 2007, *Baltic Astronomy*, 16, 26
- Press, W. H., & Teukolsky, S. A. 1992, *Computers in Physics*, 6, 188
- Ragusa, E., Rosotti, G., Teyssandier, J., et al. 2018, *MNRAS*, 474, 4460, doi: [10.1093/mnras/stx3094](https://doi.org/10.1093/mnras/stx3094)
- Ramstedt, S., Mohamed, S., Vlemmings, W. H. T., et al. 2017, *A&A*, 605, A126, doi: [10.1051/0004-6361/201730934](https://doi.org/10.1051/0004-6361/201730934)
- Roulston, B. R., Green, P. J., Ruan, J. J., et al. 2019, *ApJ*, 877, 44, doi: [10.3847/1538-4357/ab1a3e](https://doi.org/10.3847/1538-4357/ab1a3e)
- Sabach, E., & Soker, N. 2018, *MNRAS*, 473, 286, doi: [10.1093/mnras/stx2377](https://doi.org/10.1093/mnras/stx2377)
- Sahai, R., Findeisen, K., Gil de Paz, A., & Sánchez Contreras, C. 2008, *ApJ*, 689, 1274, doi: [10.1086/592559](https://doi.org/10.1086/592559)
- Saladino, M. I., & Pols, O. R. 2019, *A&A*, 629, A103, doi: [10.1051/0004-6361/201935625](https://doi.org/10.1051/0004-6361/201935625)
- Saladino, M. I., Pols, O. R., & Abate, C. 2019, *A&A*, 626, A68, doi: [10.1051/0004-6361/201834598](https://doi.org/10.1051/0004-6361/201834598)
- Saladino, M. I., Pols, O. R., van der Helm, E., Pelupessy, I., & Portegies Zwart, S. 2018, *A&A*, 618, A50, doi: [10.1051/0004-6361/201832967](https://doi.org/10.1051/0004-6361/201832967)
- Van Winckel, H., Waelkens, C., Waters, L. B. F. M., et al. 1998, *A&A*, 336, L17
- Vlemmings, W., Khouri, T., O’Gorman, E., et al. 2017, *Nature Astronomy*, 1, 848, doi: [10.1038/s41550-017-0288-9](https://doi.org/10.1038/s41550-017-0288-9)
- Woitke, P. 2006a, *A&A*, 460, L9, doi: [10.1051/0004-6361:20066322](https://doi.org/10.1051/0004-6361:20066322)
- . 2006b, *A&A*, 452, 537, doi: [10.1051/0004-6361:20054202](https://doi.org/10.1051/0004-6361:20054202)

APPENDIX

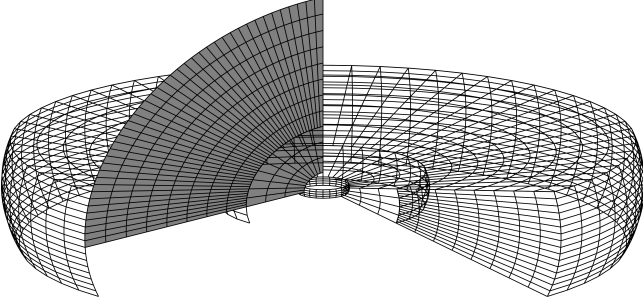


Figure 8. An illustrative picture of the spherical mesh of the equatorial region. Angular resolution doubles in both polar and azimuthal coordinates in the outer region. The figure is only for illustration, the resolution of our simulation is shown in Table 5.

A. OPTICAL DEPTH

$\tau(x, y, z)$ is calculated by interpolating $\tau(r, \theta, \phi)$ linearly after translating (x, y, z) to the frame whose origin is the center of the primary star. $\tau(r, \theta, \phi)$ is the optical depth trace back to an angular dependent surface $r_{\text{surf}}(\theta_j, \phi_k)$ that encloses the photosphere and probably the chromosphere of the primary star. For simplicity, r_{surf} is defined as the smallest contour of $\rho = 10^{-10} \text{ g cm}^{-3}$ that encloses the AGB star. τ is defined on a discrete spherical coordinate

$$\tau(r_i, \theta_j, \phi_k) = \begin{cases} \tau_{\text{inside}} & r_i < r_{\text{surf}}, \\ \int_{r_{\text{surf}}}^{r_i} \kappa(r, \theta_j, \phi_k) \rho(r, \theta_j, \phi_k) dr & r_i \geq r_{\text{surf}}, \end{cases} \quad (\text{A1})$$

where $\theta_j \in [0, \pi]$ is the discretized polar angle and $\phi_k \in [0, 2\pi]$ is the discretized azimuthal angle. τ_{inside} is a large number but is irrelevant to the actual calculation because a_{rad} is set to 0 within r_{surf} . To distinguish, we will call a finite volume in Cartesian coordinate a 'cell' and a finite volume in spherical coordinate a 'bin' as shown in Figure 8. The center of this spherical coordinate is at the center of the primary star therefore the coordinate is translated. $\kappa(r_i, \theta_j, \phi_k)$ and $\rho(r_i, \theta_j, \phi_k)$ are mapping and regriding of the data in the translated Cartesian coordinate. To distinguish the translated Cartesian coordinate from the untranslated coordinate, we use (x', y', z') to denote the translated Cartesian coordinate. The density of a bin in the spherical coordinate is defined as

$$\rho(r_i, \theta_j, \phi_k) = \frac{\sum \rho(x', y', z') dv(x', y', z') \delta(x', y', z')}{\sum dv(x', y', z') \delta(x', y', z')}, \quad (\text{A2})$$

where dv is the finite volume in the corresponding coordinate and $\delta(x', y', z')$ can be thought of as a kernel

function, i.e.,

$$\delta(x', y', z') \begin{cases} 1 & \text{if } (x', y', z') \in dv(r_i, \theta_j, \phi_k), \\ 0 & \text{if } (x', y', z') \notin dv(r_i, \theta_j, \phi_k). \end{cases} \quad (\text{A3})$$

The membership relation \in can be defined explicitly as,

$$r_{i-1/2} \leq r < r_{i+1/2}, \quad (\text{A4})$$

$$\theta_{j-1/2} \leq \theta < \theta_{j+1/2}, \quad (\text{A5})$$

$$\phi_{k-1/2} \leq \phi < \phi_{k+1/2}, \quad (\text{A6})$$

where (r, θ, ϕ) is the spherical coordinate of (x', y', z') .

Similarly, we define the opacity of a bin as mass weighted average

$$\kappa(r_i, \theta_j, \phi_k) = \frac{\sum \rho(x', y', z') \kappa(x', y', z') dv(x', y', z') \delta(x', y', z')}{\sum \rho(x', y', z') dv(x', y', z') \delta(x', y', z')}. \quad (\text{A7})$$

In the mapping and regriding process, the computational domain is divided into two regions, one is the polar region and the other is the equatorial region. The polar region does not resolve the azimuthal angle, therefore, in the polar region, Equation A3 becomes

$$\delta(x', y', z') \begin{cases} 1 & \text{if } (x', y', z') \in dv(r_i, \theta_j), \\ 0 & \text{if } (x', y', z') \notin dv(r_i, \theta_j). \end{cases} \quad (\text{A8})$$

The equatorial region resolves the azimuthal angle. Angular resolution is increased for both two regions as r gets larger. We illustrate the spherical grid that is used for the radiative transfer in Figure 8. The resolution structure that we use is listed in Table 5.

Inner region			Refined region		
$r \in [1.25, 2.5] \text{ AU}$			$r \in [2.5, 36] \text{ AU}$		
dr	dθ	dφ	dr	dθ	dφ
0.05AU	π/50	π/50	0.05AU	π/100	π/100

Table 5. Angular resolution of the equatorial region in radiative transfer. The polar region has the same angular resolution except that azimuthal angle is not resolved.

In Section 2.2, we calculate the dust-free optical depth by setting $\kappa = \kappa_{\text{mol}} = 2.5 \times 10^{-4} \text{ g cm}^{-3}$ everywhere. The $\tau(r, \theta, \phi)$ for the radiation-hydrodynamic simulation is re-calculated by using the adopted opacity profile in Section 2.4.

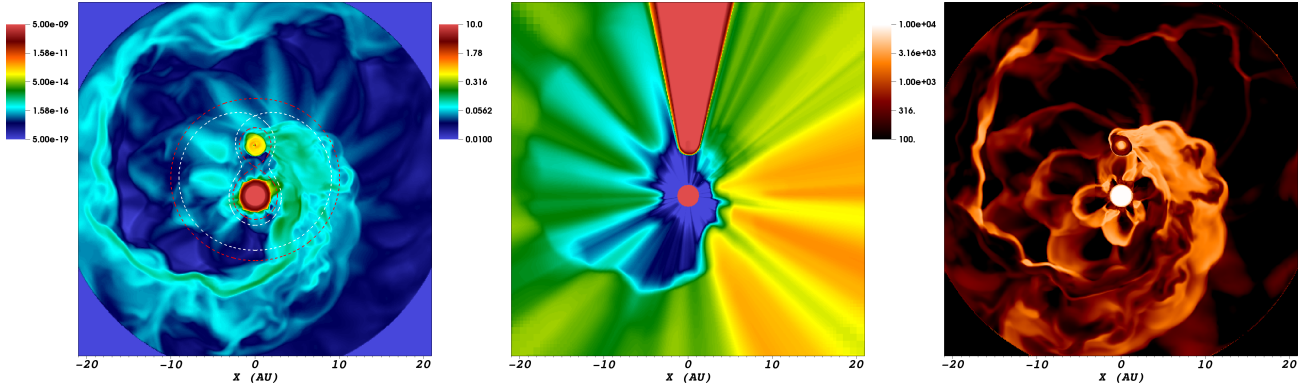


Figure 9. The snapshots for 6.0 AU binaries simulations without accretion in XY plane at $Z = 0$ for ρ [$\text{g}\cdot\text{cm}^{-3}$], τ , and T [K] (from the left to right). The snapshots is provided at 1.91 orbits. In density plots we also show L_1 potential with red dashed lines and L_2 potential with a white dashed line.

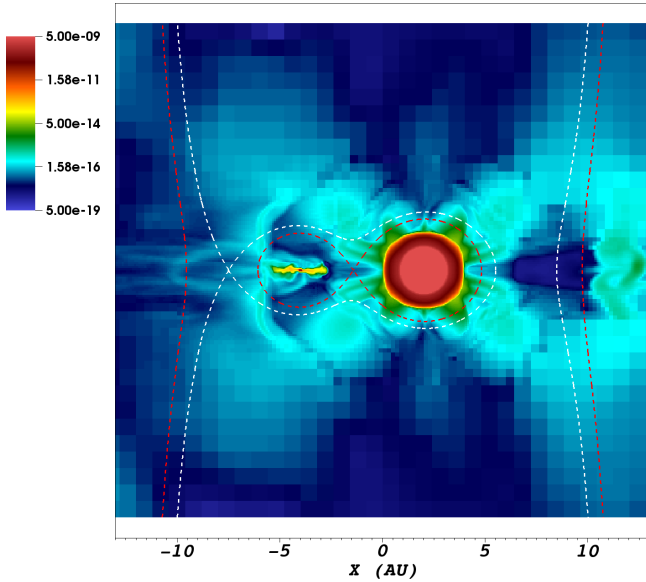


Figure 10. The snapshots for 6.0 AU binaries simulations without accretion in XZ plane at $Y = 0$ for ρ [$\text{g}\cdot\text{cm}^{-3}$]. The snapshots is provided at 1.91 orbits. We also show L_1 potential with red dashed lines and L_2 potential a white dashed line.

B. DISK AROUND SECONDARY WITHOUT ACCRETION

Figure 9 shows a binary simulation of $d = 6.0\text{AU}$ with everything the same as the one in Section 6.2 except that the accretion of the secondary is turned off. We find a disk appears around the secondary and the secondary cast a strong shadow in the line of sight of the AGB star. There is also a high temperature bow shock in the temperature plot. In Figure 10, we can see that the disk around the secondary is thin.